



**HAL**  
open science

**Equivalence between dynamic mode decomposition and temporal discrete Fourier transform for zero mean numerical and experimental data. Analytical solution. Applications to 3D CFD results and to experimental films**

Frédéric Lévy

► **To cite this version:**

Frédéric Lévy. Equivalence between dynamic mode decomposition and temporal discrete Fourier transform for zero mean numerical and experimental data. Analytical solution. Applications to 3D CFD results and to experimental films. 2021. hal-03034486v2

**HAL Id: hal-03034486**

**<https://hal.science/hal-03034486v2>**

Preprint submitted on 29 Nov 2021 (v2), last revised 21 Dec 2023 (v4)

**HAL** is a multi-disciplinary open access archive for the deposit and dissemination of scientific research documents, whether they are published or not. The documents may come from teaching and research institutions in France or abroad, or from public or private research centers.

L'archive ouverte pluridisciplinaire **HAL**, est destinée au dépôt et à la diffusion de documents scientifiques de niveau recherche, publiés ou non, émanant des établissements d'enseignement et de recherche français ou étrangers, des laboratoires publics ou privés.

# Equivalence between dynamic mode decomposition and temporal discrete Fourier transform for zero mean numerical and experimental data. Analytical solution. Applications to 3D CFD results and to experimental films.

Frédéric Lévy <sup>a</sup>

<sup>a</sup> DMPE, ONERA, Université Paris Saclay, F-91123 Palaiseau, France

---

## ARTICLE INFO

## ABSTRACT

The equivalence between dynamic mode decomposition and discrete Fourier transform for numerical and experimental data, the mean of which in each set equals zero, is used to propose an analytical solution for the DMD, which is equivalent to the equations for the DFT. This solution is an exact solution, based on the reduction of all the snapshots by the mean of the whole sequence, which is also the rigid mode (not time dependant) of the considered sequence. The sampling time step is assumed to be constant. The time dependant evolution of the modal shapes is a linear combination of all the reduced snapshots, the weight functions being the results of the analytical solution. The frequency of each mode remains constant in the time. No matrix processing is required to describe the modal behaviour of the sequence. The error of this DMD analysis solution comes only from the data themselves : the time step, the snapshots number, and the snapshots values. This simple solution allows to process in a quite short time a great amount of data, the limit of which is the computer RAM size. Dealing with a great number of snapshots allows, in one hand, to compensate some disadvantages outlined for the DFT, and on the other hand, to bring out better the preponderant modes and to make continuous videos of the selected modes shapes. After an academic validation case, typically unsteady and transient, dealing with 50000 snapshots and 125000 values per snapshot, two application examples of this DMD analysis solution are then presented : the first one concerns some 3D CFD results (25500 snapshots, 289000 values per snapshot), and the second one concerns the images extracted from two experimental films (16000 snapshots, 524000 values per snapshot).

---

## 1. Introduction

Based on the Koopman analysis of nonlinear dynamical systems [1], the « dynamic mode decomposition » technique was introduced by Rowley *et al.* [2] and Schmid [3], as a numerical procedure for extracting dynamical features from flow data.

DMD computes a set of modes, the frequency of which remains constant in the time. The method highlights the major periodic phenomena, and permits to reconstruct the signal by choosing the most representative modes. It is based on data (experimental or CFD results) whose equations generating them are not known a priori. The modes are not orthogonal between each other, but their time dependant evolution can be physically meaningful.

To extract the dynamic features of the snapshots, some important matrix processings, such as the QR decomposition [3, 4, 5], or the Single Value Decomposition [3, 6, 7] are commonly used. However, they require some advanced resolution techniques as well as some important computer resources. The efficient and accurate method proposed by Drmac *et al.* [8] does not mention any information about this last point, but it is not unreasonable to think this method requires some important computer resources as well.

The purpose of the author was to find a resolution method for DMD which sets free from any matrix processing, and to reduce significantly the computing time, in particular when the snapshots number and the values number per snapshot are high. A few years after the introduction of the DMD, Chen *et al.* [9] have outlined a possibility to subtract the snapshots mean to all the snapshots, and they showed this operation leads to an exact reduction of the DMD to the temporal discrete Fourier transform. Although they mentioned this result is undesirable, explaining the implications of the mean subtraction, it is used here again to extract frequencies and spatial structures from fluid mechanics data. The notion of modal growth rate is therefore abandoned.

After a theoretical reminder of this modified DMD method, where an analytic solution is proposed, the equivalence with temporal DFT is recalled, and some arguments to compensate some disadvantages are presented.

An academic validation case, typically unsteady and transient, with 50000 snapshots and 125000 values per snapshot is presented. It is followed by two application examples : the first one concerns some 3D CFD results (25500 snapshots, 289000 values per snapshot), and the second one concerns the images extracted from two experimental films (16000 snapshots, 524000 values per snapshot).

## 2. Theoretical reminder

The solution of the DMD method in this paper is based on a definition of DMD as an algorithm applied to a sequential snapshot set. It is not the most general definition of DMD, which was written by Tu [10], but is often useful for theoretical analyses.

### 2.1 Description

$N + 1$  snapshots are considered :  $\mathbf{v}_0, \mathbf{v}_1, \mathbf{v}_2, \dots, \mathbf{v}_N$ . A vector  $\mathbf{v}_j$  stands for the field of a variable which describes the calculated flow or the experimental data at the instant of index  $j$  ( $0 \leq j \leq N$ ). As it is mentioned in quite a lot of articles, the mean value of all the snapshots, a vector noted  $\bar{\mathbf{v}}$ , is introduced [3, 7, 9-14] :

$$\bar{\mathbf{v}} = \frac{\sum_{i=0}^N \mathbf{v}_i}{N+1} \quad (2.1)$$

The relation (2.1) is written again in order to bring out the subtraction of the mean vector to all the snapshots [9, 13] :

$$\mathbf{v}_N - \bar{\mathbf{v}} = N\bar{\mathbf{v}} - \sum_{i=0}^{N-1} \mathbf{v}_i = -\sum_{i=0}^{N-1} (\mathbf{v}_i - \bar{\mathbf{v}}) \quad (2.2)$$

Defining the rigid mode, mentioned in the abstract, as the mean value of all the snapshots, this operation is then equivalent to consider only the fluctuations of the snapshots around the rigid mode, which remains the same during the whole sequence (its frequency is equal to zero). This rigid mode depends on the sequence itself, since it may change if the considered time interval changes. Defining the matrix  $\mathbf{D}_0^{N-1}$  and  $\mathbf{D}_1^N$  as  $\mathbf{D}_0^{N-1} = \{\mathbf{v}'_0, \mathbf{v}'_1, \mathbf{v}'_2, \dots, \mathbf{v}'_{N-1}\}$  and  $\mathbf{D}_1^N = \{\mathbf{v}'_1, \mathbf{v}'_2, \dots, \mathbf{v}'_{N-1}, \mathbf{v}'_N\}$ , with  $\mathbf{v}'_i = \mathbf{v}_i - \bar{\mathbf{v}}$ , the relation (2.2) can be synthesized into the expression :

$$\mathbf{D}_1^N = \mathbf{D}_0^{N-1} \mathbf{S} \quad (2.3)$$

$\mathbf{S}$  is a companion type square matrix :

$$\mathbf{S} = \begin{pmatrix} 0 & \cdots & \cdots & 0 & -1 \\ 1 & 0 & & \vdots & -1 \\ 0 & 1 & \ddots & \vdots & \vdots \\ \vdots & \ddots & \ddots & 0 & -1 \\ 0 & \cdots & 0 & 1 & -1 \end{pmatrix}_{N,N} \quad (2.4)$$

The DMD analysis is based on the spectral decomposition of the companion matrix, which appears here to be very simple. The characteristic polynomial of  $\mathbf{S}$  is :

$$P_N(x) = x^N + x^{N-1} + \dots + x + 1 = \frac{x^{N+1} - 1}{x - 1} \quad (2.5)$$

The roots of  $P_N$ , noted  $x_p$ , are then the  $(N+1)^{\text{st}}$  roots of unity, excepted unity :

$$x_p = \exp\left(\frac{2i p \pi}{N+1}\right) \quad p = 1 \text{ to } N \quad (2.6)$$

These roots are the eigenvalues of  $\mathbf{S}$ . The sampling time step is used to link them to the modal frequencies. Assuming the sampling time step as a constant is involved in the building of the DMD theory [3] (the sequence of

data is then formulated as a Krylov sequence, two consecutive snapshots of which are connected by an operator which is supposed linear, in the aim to create a linear combination between the first  $N$  snapshots, assuming they are independent, and the last one, when  $N$  is high enough to make reasonable such an operation).

## 2.2 Expression of the eigenvalues

A modified expression for the eigenvalues, noted  $\lambda_p$ , is determined such as the argument is included between  $-\pi$  and  $\pi$  ( $-\pi$  excluded), to let appear the conjugate eigenvalues. An integer  $m$  is introduced : if  $N$  is even,  $m = \frac{N}{2}$ .

If  $N$  is odd,  $m = \frac{N-1}{2}$ .  $\Delta t$  is the sampling time step.

$$\text{For } p = 0 \text{ to } m - 1, \quad \lambda_p = \exp\left(\frac{2i\pi(p-m)}{N+1}\right) \quad (2.7)$$

$$\text{The associated frequency is : } f_p = \frac{p-m}{(N+1)\Delta t} \quad (2.8)$$

$$\text{For } p = m \text{ to } N - 1, \quad \lambda_p = \exp\left(\frac{2i\pi(p+1-m)}{N+1}\right) \quad (2.9)$$

$$\text{The associated frequency is : } f_p = \frac{p+1-m}{(N+1)\Delta t} \quad (2.10)$$

A constant sampling time step allows here to correlate each eigenvalue with its own frequency.

## 2.3 Maximum frequency, resolution frequency

$$\text{Since } -\pi < \omega_p \Delta t \leq \pi, \text{ with } \omega_p = 2\pi f_p, \text{ then : } f_{\max} = \frac{1}{2\Delta t} \quad (2.11)$$

$$\text{The resolution frequency } \Delta f \text{ is expressed as : } \Delta f = \frac{1}{(N+1)\Delta t} \quad (2.12)$$

The tolerance around a DMD frequency is  $\Delta f / 2$ .

## 2.4 Expression of the Vandermonde matrix and its inverse

The relation  $P_N(\lambda_p) = 0$  leads to the existence of a Vandermonde matrix, noted  $\mathbf{V}$ , made up from the eigenvalues of the companion matrix, and which is a left eigenvector basis of  $\mathbf{S}$  :

$$\mathbf{V}\mathbf{S} = \mathbf{A}\mathbf{V} \quad (2.13)$$

$$\mathbf{V} = \begin{pmatrix} 1 & \lambda_0 & \lambda_0^2 & \cdots & \lambda_0^{N-1} \\ 1 & \lambda_1 & \lambda_1^2 & \cdots & \lambda_1^{N-1} \\ \vdots & \vdots & \vdots & & \vdots \\ 1 & \lambda_{N-1} & \lambda_{N-1}^2 & \cdots & \lambda_{N-1}^{N-1} \end{pmatrix} \quad (2.14)$$

$\mathbf{A}$  is the eigenvalues matrix :  $\mathbf{A} = \text{diag}(\lambda_0, \dots, \lambda_{N-1})$ . The elements can be linked with time since the sampling time step is constant. In that case, the Vandermonde matrix columns are linked to a time dependant evolution, while the lines are linked to a modal evolution [6]. With the relations (2.7) and (2.9), the elements of Vandermonde matrix are derived immediately (line index  $p = 0$  to  $N-1$ , column index  $q = 0$  to  $N-1$ ) :

$$p < m \quad \lambda_p^q = \exp\left(\frac{2i\pi q(p-m)}{N+1}\right) \quad (2.15)$$

$$p \geq m \quad \lambda_p^q = \exp\left(\frac{2i\pi q(p+1-m)}{N+1}\right) \quad (2.16)$$

Since the eigenvalues of the companion matrix are simple, the Vandermonde matrix is invertible. Therefore, we can write :

$$\mathbf{S} = \mathbf{V}^{-1} \mathbf{A} \mathbf{V} \quad (2.17)$$

To calculate the expression of the elements of the Vandermonde matrix inverse, which are noted  $b_{ij}$ , the matrix  $\mathbf{V}^{-1}$  is written as a right eigenvector basis of the matrix  $\mathbf{S}$ :

$$\mathbf{S} \mathbf{V}^{-1} = \mathbf{V}^{-1} \mathbf{A} \quad (2.18)$$

Then this property is developed. Multiplying the relation (2.18) on the right by the unit vector  $\mathbf{e}_j$  of the  $(j + 1)^{\text{th}}$  column, some relations are derived between the elements of the column of index  $j$  of the matrix  $\mathbf{V}^{-1}$ .  $\mathbf{S} (\mathbf{V}^{-1} \mathbf{e}_j) = \mathbf{V}^{-1} (\mathbf{A} \mathbf{e}_j)$  is equivalent to :

$$\begin{pmatrix} 0 & 0 & \cdots & 0 & a_0 \\ 1 & 0 & & \vdots & a_1 \\ 0 & 1 & \ddots & \vdots & \vdots \\ \vdots & \ddots & \ddots & 0 & a_{N-2} \\ 0 & \cdots & 0 & 1 & a_{N-1} \end{pmatrix} \times \begin{pmatrix} b_{0,j} \\ b_{1,j} \\ \vdots \\ b_{N-2,j} \\ b_{N-1,j} \end{pmatrix} = \lambda_j \begin{pmatrix} b_{0,j} \\ b_{1,j} \\ \vdots \\ b_{N-2,j} \\ b_{N-1,j} \end{pmatrix} \quad (2.19)$$

The relation (2.19) yields :

$$0 \leq i < N-1 \quad b_{ij} = b_{N-1,j} \times \frac{\lambda_j^{N-i} - 1}{\lambda_j - 1} \quad (2.20)$$

As the relation (2.20) gives the coefficients  $b_{ij}$  by a constant, the identity  $\mathbf{V} \mathbf{V}^{-1} = \mathbf{I}$  is used to provide the closure relation :

$$\sum_{k=0}^{N-1} \lambda_i^k b_{kj} = \delta_{ij} \quad (\delta_{ij} \text{ is the Kronecker symbol}) \quad (2.21)$$

Knowing that  $\lambda_p^{N+1} = 1$ , the elements  $b_{ij}$  of the matrix  $\mathbf{V}^{-1}$  (line index  $i = 0$  to  $N-1$ , column index  $j = 0$  to  $N-1$ ) are deduced :

$$b_{ij} = \frac{\lambda_j (\lambda_j^{N-i} - 1)}{N + 1} \quad (2.22)$$

The identities  $\mathbf{V} \mathbf{V}^{-1} = \mathbf{I}$  (when  $\delta_{ij} = 0$ ) and  $\mathbf{V}^{-1} \mathbf{V} = \mathbf{I}$  can be checked with the help of the relations  $\sum_{k=0}^{N-1} \lambda_p^k = -\frac{1}{\lambda_p}$  ( $p = 0$  to  $N-1$ ), and  $1 + \sum_{k=0}^{N-1} \lambda_k^q = 0$  with  $0 < |q| \leq N$ .

## 2.5 Modal matrix

Combining the relations (2.3) and (2.17), appears the matrix  $\mathbf{W} = \mathbf{D}_0^{N-1} \mathbf{V}^{-1}$ , allowing to write the matrix  $\mathbf{D}_1^N$  as the product :

$$\mathbf{D}_1^N = \mathbf{W} \mathbf{A} \mathbf{V} \quad (2.23)$$

The columns of  $\mathbf{W}$  are noted  $\mathbf{w}_p$  ( $p = 0$  to  $N-1$ ) :

$$\mathbf{w}_p = \sum_{k=0}^{N-1} \mathbf{v}'_k b_{kp} = \sum_{k=0}^{N-1} \mathbf{v}'_k \frac{\lambda_p (\lambda_p^{N-k} - 1)}{N + 1} \quad \text{with} \quad \mathbf{v}'_k = \mathbf{v}_k - \bar{\mathbf{v}} \quad (2.24)$$

The relation (2.23) is equivalent to the expression :

$$\text{For } j = 0 \text{ to } N-1, \quad \sum_{p=0}^{N-1} \mathbf{w}_p \lambda_p^{j+1} = \mathbf{v}'_{j+1} \quad (2.25)$$

At the time  $t = 0$ , associated with  $j = -1$  in the relation (2.25), the identity  $\mathbf{V}^{-1} \mathbf{V} = \mathbf{I}$  is used.

$$\mathbf{V}^{-1} \mathbf{V} = \mathbf{I} \Leftrightarrow \sum_{k=0}^{N-1} b_{ik} \lambda_k^j = \delta_{ij} \quad (2.26)$$

$$\sum_{p=0}^{N-1} \mathbf{w}_p = \sum_{p=0}^{N-1} \left( \sum_{k=0}^{N-1} \mathbf{v}'_k b_{kp} \right) = \sum_{k=0}^{N-1} \mathbf{v}'_k \left( \sum_{p=0}^{N-1} b_{kp} \right) = \sum_{k=0}^{N-1} \mathbf{v}'_k \delta_{k0} = \mathbf{v}'_0 \quad (2.27)$$

The vector  $\mathbf{w}_p$  is the complex shape of the mode  $p$  at the time  $t = 0$ . Since the matrix  $\mathbf{W}$  contains all the vectors  $\mathbf{w}_p$ , it can be named a modal matrix.

### 2.6 Time dependant evolution of the modes

Using the matrix  $\mathbf{W}$  and  $\mathbf{A}$ , the whole time dependant evolution of the snapshots can be rebuilt. In particular for one specific mode, if it is preponderant in front of other modes. In that case, since the components of the final shapes are real values, the time dependant evolution of the shape of the mode  $p$ , the eigenvalue of which  $\lambda_p$  is complex, must be computed with the time dependant evolution of the shape of the mode  $q$ , where  $\lambda_q$  is the conjugate eigenvalue of  $\lambda_p$ . If  $\lambda_q = \bar{\lambda}_p$ , then  $b_{kq} = \bar{b}_{kp}$  and  $\mathbf{w}_q = \bar{\mathbf{w}}_p$ . The column of index  $q$  in  $\mathbf{V}^{-1}$  is the conjugate column of the column of index  $p$ . As a result, the vector  $\mathbf{w}_p \lambda_p^j + \mathbf{w}_q \lambda_q^j$ , the elements of which are real, represents the total contribution of the mode at the positive frequency  $f_p$  (relation (2.10)) at the time of index  $j$  ( $j = 0$  to  $N$ ). The amplitude of the mode  $p$  at the instant  $j$  is the Euclidean norm of this vector.

$$\mathbf{w}_p \lambda_p^j + \mathbf{w}_q \lambda_q^j = 2 \operatorname{Re}(\mathbf{w}_p \lambda_p^j) = \frac{2}{N+1} \left( \sum_{k=0}^{N-1} \mathbf{v}'_k \operatorname{Re}(\lambda_p^{j-k} - \lambda_p^{j+1}) \right) \quad (2.28)$$

The time dependant evolution of the shape of the mode  $p$ , the pulsation of which is  $\omega_p = 2\pi f_p$ , is given eventually by the expression :

$$\boxed{\mathbf{w}_p \lambda_p^j + \mathbf{w}_q \lambda_q^j = \frac{2}{N+1} \left( \sum_{k=0}^{N-1} \mathbf{v}'_k (\cos(\omega_p (j-k)\Delta t) - \cos(\omega_p (j+1)\Delta t)) \right)} \quad (2.29)$$

Or, with  $t_j = j \Delta t$  ( $j = 0$  to  $N$ ) and  $t_k = k \Delta t$  :

$$\boxed{\mathbf{w}_p \lambda_p^j + \mathbf{w}_q \lambda_q^j = \frac{2}{N+1} \left( \sum_{k=0}^{N-1} \mathbf{v}'_k (\cos(\omega_p (t_j - t_k)) - \cos(\omega_p (t_j + \Delta t))) \right)} \quad (2.30)$$

The time dependant evolution of the modal shapes is obtained directly from the reduced snapshots, weighted by a simple time dependant function. Therefore it is no longer necessary to calculate the Vandermonde matrix, its inverse, and the modal matrix. The amplitude of the mode of frequency  $f_p$  at the time  $t_j$  is still the Euclidean norm of the vector given by the relation (4.18).

### 2.7 Comments

The eigenvalues are completely independent of the data. They depend only on the snapshots number, and the spectral resolution is uniform, like the one obtained by a Fourier transform. This is a result for a DMD analysis made on fluctuating data (removing the mean of the original data), which is usually considered as a disadvantage, compared to a DMD analysis made on the raw data (without subtracting the mean), leading to a non-uniform spectral resolution [3, 6, 9]. In both cases, the resolution frequency decreases with an increase of the snapshots number. However, the value of a modal frequency is necessarily associated with a tolerance around this value, because the real value may not be usually exactly predicted. With a variable resolution frequency, this tolerance may be awkward to calculate. With a unique resolution frequency, the tolerance is very simple (half of the resolution frequency). In addition, in order to approach the real value of a modal frequency, the tolerance must decrease. Increasing the

snapshots number is a convenient possibility. Increasing the sampling time step is not relevant, because some information about the researched physical phenomena can be lost.

By construction of the eigenvalues, the Nyquist condition is implicitly respected. The mean-subtraction sets free from any constraint about a minimum number of snapshots, since the method works regardless of the number and the values of the snapshots. In practice, a DMD analysis leads of course to a much better result with a high number of snapshots (see section 3). With this DMD method equivalent to DFT, the solution is an exact solution, since the coefficients of the last column of the companion matrix  $\mathbf{S}$  are all equal to -1, and analytic, under the relations (2.15), (2.16) and (2.22). No more matrix processing is required to get the results. This analytical solution sets completely free from the constraint to operate such processings, which are expensive in time calculation and in memory size if  $N$  is high. The error of this DMD analysis method comes only from the data themselves : the time step, the snapshots number, and the snapshots values. This simple solution processes in a short time a quite great amount of data, the limit of which is the computer RAM.

The notion of amplified or damped modes, as it is common in the original DMD analysis, does not exist here, since all the eigenvalues have a unit magnitude. The obtained modes are just preponderant or not. We must keep in mind that the notion of modal growth rate is valid only in the time window of the data sequence, since the calculation does not know what happens physically before the first snapshot and after the last one. Whatever the original DMD method can reveal about this dynamical information, it is limited in the time of the observed data. Therefore, it is not unreasonable to turn towards a method, although equivalent to DFT, which presents some other significant advantages, as long as the right preponderant modes of any sequence are still detected. An example of a typical unsteady and transient case treated with this DMD method is presented in section 3. It comes out its preponderant modes are determined correctly.

In addition, with the original DMD method, it is known that the local frequency resolution around the frequency of interest depends both on the snapshots number and the last snapshot [6, 9]. This last snapshot strongly influences the quality of the DMD analysis, and no rules can be deduced for an appropriate choice of the snapshot sequence and the frequency resolution [6]. This problem does not arise with this DMD method equivalent to DFT.

In the end, the great advantage of the DMD is the possibility to make visible the time dependant evolution of the shapes of the selected preponderant modes. The time dependant evolution of a mode is equivalent to a time dependant deformation of its initial shape to a certain frequency with an optional phase shift.

## 2.8 Equivalence between DMD with subtraction of the mean flow and DFT

Using  $\lambda_p^{N+1} = 1$  and  $\mathbf{v}'_N = -\sum_{k=0}^{N-1} \mathbf{v}'_k$ , the expression (2.24) is written in a different way, which leads to a direct DFT of the reduced snapshots ( $\mathbf{v}'_k = \mathbf{v}_k - \bar{\mathbf{v}}$ ) :

$$\begin{aligned} \text{For } p = 0 \text{ to } N-1, \quad \mathbf{w}_p &= \sum_{k=0}^{N-1} \mathbf{v}'_k \frac{\lambda_p (\lambda_p^{N-k} - 1)}{N+1} = \frac{1}{N+1} \left( \sum_{k=0}^{N-1} \mathbf{v}'_k \lambda_p^{-k} - \lambda_p \sum_{k=0}^{N-1} \mathbf{v}'_k \right) = \frac{1}{N+1} \left( \sum_{k=0}^N \mathbf{v}'_k \lambda_p^{-k} - \mathbf{v}'_N \lambda_p^{-N} + \lambda_p \mathbf{v}'_N \right) \\ \Rightarrow \quad \mathbf{w}_p &= \frac{1}{N+1} \sum_{k=0}^N \mathbf{v}'_k \lambda_p^{-k} \end{aligned} \quad (2.31)$$

It is possible to add the vector  $\mathbf{w}_N = \frac{1}{N+1} \sum_{k=0}^N \mathbf{v}'_k \lambda_N^{-k}$ . If the  $N$  eigenvalues given by the relations (2.7) and (2.9) are all different from unity, then the  $(N+1)^{\text{st}}$  root, noted  $\lambda_N$ , equals unity. Therefore,  $\mathbf{w}_N$  is zero, and we can write :

$$\text{For } p = 0 \text{ to } N, \quad \mathbf{w}_p = \frac{1}{N+1} \sum_{k=0}^N \mathbf{v}'_k \lambda_p^{-k} \quad (2.32)$$

By construction of the matrix  $\mathbf{W}$ , the relations (2.25) and (2.27) are equivalent to the inverse DFT of the modal vectors  $\mathbf{w}_p$  :

$$\text{For } j = 0 \text{ to } N, \quad \mathbf{v}'_j = \sum_{p=0}^{N-1} \mathbf{w}_p \lambda_p^j = \sum_{p=0}^N \mathbf{w}_p \lambda_p^j \quad (2.33)$$

After an application to an academic case, submitted successfully to a DMD analysis with the analytical solution to validate the method, two practical cases were selected to present some application results : the first case concerns some 3D CFD results, and the second case concerns the images extracted from two experimental films. Both cases are in current use in the field of fluid mechanics research.

### 3. Application to an academic validation case

#### 3.1 Context

The DMD code, built with the analytical solution, is tested to find the acoustic modes of a 2D cavity. The cavity is rectangular. The length (1 m) is noted  $L$ , the width (50 cm) is noted  $h$  (figure 1). It is closed at one extremity in the length direction (at the abscissa origin), and open at the other one. It is filled with still air at ambient conditions. A pressure impulse is introduced at the initial instant within the cavity, and the waves propagation and reflections which develop inside are observed. This case is typically unsteady and transient, since the pressure impulse vanishes while the additional mass contained in the impulse is evacuated gradually at the exit on the right side of the cavity, until the ambient pressure is reached everywhere inside the cavity (theoretically at the end of an infinite time).

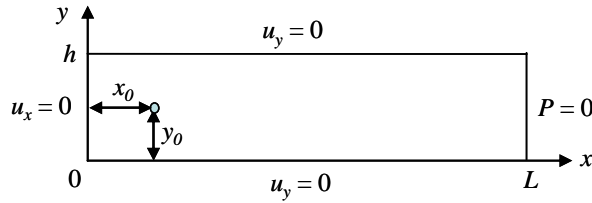


Fig. 1. Schema of the 2D cavity.

The central position of the pressure impulse is on the median line of the cavity at  $y_0 = h/2$  and at  $x_0 = 2$  cm from the left wall. The impulse pressure is applied in a 8 mm square centred at the point  $(x_0, y_0)$  and oriented like the rectangle of the cavity. The fluid is inviscid and non turbulent.

#### 3.2 Theoretical solution

Without any friction during the waves propagation, the flow remains isentropic. Therefore, the classical governing equations linearized for small perturbations (the second order terms are neglected) in a still fluid are [15] :

$$\Delta P - \frac{1}{c_0^2} \frac{\partial P}{\partial t} = 0 \quad \text{and} \quad \frac{\partial \mathbf{v}}{\partial t} = -\frac{1}{\rho_0} \nabla P \quad (3.1)$$

The pressure  $P$  and the velocity  $\mathbf{v}$ , the components of which are noted  $u$  and  $v$ , represent the small perturbations around their mean values. The mean pressure is the ambient pressure. The mean velocity vector is null. Therefore, the mean density  $\rho_0$  and the sound velocity  $c_0$  are constant ( $c_0 = 347.2$  m/s). The boundary conditions are :

$$\begin{aligned} x = 0 & & u = 0 & \Leftrightarrow & \partial P / \partial x = 0 \\ x = L & & P = 0 & & \\ y = 0 \text{ and } y = h & & v = 0 & \Leftrightarrow & \partial P / \partial y = 0 \end{aligned}$$

The pressure perturbation inside the cavity is then expressed in the form of a series of modes with two integers  $(n, p)$ , the frequency of which is noted  $f_{n,p}$  [15] :

$$P(x, y, t) = \sum_{n,p \geq 0} A_{n,p} \cos(\omega_{n,p} t) \cos\left(\left(n + \frac{1}{2}\right) \frac{\pi x}{L}\right) \cos\left(\frac{p \pi y}{h}\right) \quad (3.2)$$

$$\text{with } \omega_{n,p} = 2\pi f_{n,p} \quad \text{and} \quad \boxed{f_{n,p} = \frac{c_0}{2} \sqrt{\frac{(2n+1)^2}{4L^2} + \frac{p^2}{h^2}}} \quad (3.3)$$

The theoretical frequencies of the 13 first acoustic modes of the cavity are written in the table 1. The  $A_{n,p}$  coefficients are calculated on one side by integrating the pressure shape at the initial instant within the whole cavity with the space weight functions of the relation (3.2), and on the other side, by using the orthogonality property of these weight functions in their space integration within the cavity [15]. The initial pressure impulse, noted  $\delta P$ ,



is 1000 Pa (about 1 % of the ambient pressure). The square side, where  $\delta P$  is applied, is noted  $2 \varepsilon$  (thus  $\varepsilon = 4$  mm). The expression of the  $A_{n,p}$  coefficients is eventually :

$$\text{if } p = 0, \quad A_{n,0} = \frac{4 \varepsilon \delta P}{h} g(n) \quad (3.4)$$

$$\text{if } p \text{ is even and } p > 0, \quad A_{n,p} = \frac{4 \delta P (-1)^{p/2} \sin\left(\frac{p \pi \varepsilon}{h}\right)}{p \pi} g(n) \quad (3.5)$$

$$\text{with} \quad g(n) = \frac{4 \sin\left(\left(n + \frac{1}{2}\right) \frac{\pi \varepsilon}{L}\right) \cos\left(\left(n + \frac{1}{2}\right) \frac{\pi x_0}{L}\right)}{\left(n + \frac{1}{2}\right) \pi} \quad (3.6)$$

$$\text{if } p \text{ is odd,} \quad A_{n,p} = 0$$

### 3.3 Mesh used for the DMD analysis

A structured mesh is used. The cell size in both directions is 2 mm, which leads to 500 cells in the longitudinal direction and 250 cells in the transversal direction. To match the results of a CFD finite-volume code which was used afterwards for comparisons, the pressure values given by the relation (3.2) are cell-centred. Thus, each snapshot intended to the DMD analysis has 125000 values. The 8 mm square, centred at the point  $(x_0, y_0)$  and defined to receive the impulse pressure, contains therefore 16 cells around this point. Since 20 cells are usually required, in CFD computation using 2-order space schemes, to seize a wave length, this mesh is adapted to describe fluctuations up to 8680 Hz.

### 3.4 Sampling time step and resolution frequency

To capture properly the physical phenomena which will be detected by the DMD analysis, the sampling time step  $\Delta t$  is 4  $\mu$ s. The frequency resolution  $\Delta f$  for the DMD analysis is set at 5 Hz, which is quite small. Therefore, 50000 snapshots, linked here with the pressure field, must be stored ( $N = 49999$ ), the final time of the calculation is 200 ms, and the maximal frequency which can be detected by the DMD analysis is 125 kHz (section 2.3). Only the modes below 1250 Hz are studied.

### 3.5 Computer used for the DMD analysis

All the DMD analysis calculations realized for this paper were operated on a computer, each processor of which contains 24 cores Broadwell Intel® Xeon® CPU E5-2650 v4 @ 2.20GHz, a RAM of 128 GB and a total crest power of 844 GFlops.

### 3.6 DMD analysis applied to the theoretical solution

The pressure fluctuations, given by the relation (3.2), with the parameters values fixed in section 3.2, were analysed. Since the convergence of the terms in the relation (3.2), as a function of the mode frequency, towards the complete theoretical solution is very slow, only the 157 modes below 5000 Hz in the relation (3.2) were computed, which is quite enough considering the maximal frequency of the studied DMD modes.

A size of 46.73 GB in the computer RAM and a CPU time of 7h 28mn 44s were required to compute 50000 instants of the truncated theoretical solution until 200 ms, immediately followed by the amplitudes of 250 DMD modes below 1250 Hz.

The figure 2 shows the modal amplitudes of the pressure fluctuations at  $t = 0$ . The selection of the preponderant modes is made only by visual observation : the amplitude of a preponderant mode is higher than the amplitude of its neighbouring modes. Here, the figure 2 shows clearly some amplitude peaks, indicating the preponderant modes.

Below 1250 Hz, 13 preponderant modes appear. The modes the peak of which is not so high as the others indicate a significant phase shift at  $t = 0$  (their maxima appear later during their own period). The frequencies of the theoretical acoustic modes in the 2D cavity (relation (3.3)), and the frequencies detected by the DMD analysis of the truncated theoretical solution are written in the table 1. The time dependant shape of a mode is the same as the one defined by the term of the corresponding frequency in the relation (3.2).

The DMD frequencies of the computed theoretical solution equal exactly the theoretical frequencies, under the tolerance  $\Delta f / 2$  (2.5 Hz). In consequence, the DMD analysis with the exact analytical solution, equivalent to DFT, works properly to detect the right preponderant modes.

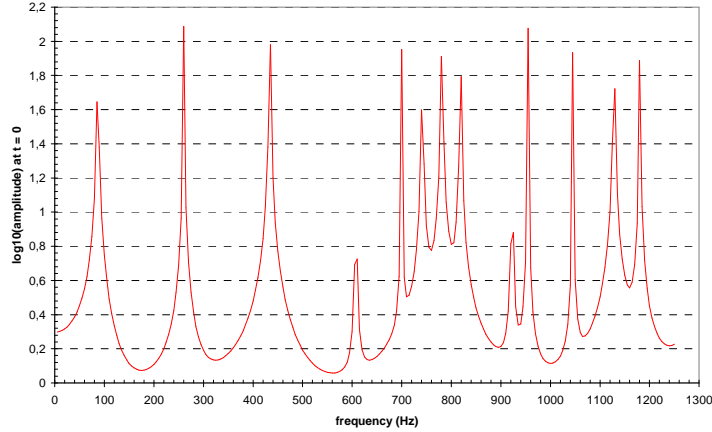


Fig. 2. Modal amplitudes of the pressure fluctuations theoretical solution at  $t = 0$ .

**Table 1**  
Acoustics modes frequencies in the 2D cavity.

theoretical frequencies (Hz)	n	p	DMD frequencies theoretical solution (Hz)	$f_{\text{DMD,TS}} - f_{\text{th}}$ (Hz)	DMD frequencies CFD flow (Hz)	$f_{\text{DMD,CFD}} - f_{\text{DMD,TS}}$ (Hz)	$f_{\text{DMD,CFD}} / f_{\text{DMD,TS}}$ (%)
86.8	0	0	85	-1.8	85	0	0
260.4	1	0	260	-0.4	255	-5	-1.923
434	2	0	435	1	425	-10	-2.299
607.6	3	0	610	2.4	595	-15	-2.459
699.804	0	2	700	0.196	685	-15	-2.143
741.62	1	2	740	-1.62	725	-15	-2.027
781.2	4	0	780	-1.2	765	-15	-1.923
818.87	2	2	820	1.13	800	-20	-2.439
922.697	3	2	925	2.303	905	-20	-2.162
954.8	5	0	955	0.2	935	-20	-2.094
1045.21	4	2	1045	-0.21	1025	-20	-1.914
1128.4	6	0	1130	1.6	1105	-25	-2.212
1180.608	5	2	1180	-0.608	1155	-25	-2.119

### 3.7 CFD flow calculation

The code CEDRE [16, 17] developed at ONERA, was used to compute the flow in the cavity with CFD code, in order to see any difference with the theoretical solution in the DMD analysis results. The mesh is described in section 3.3 (the computed quantities are cell centred). For this application, only the Euler equations were integrated by this finite-volume type code. No turbulence model. The Euler fluxes were discretized with the second-order HLLC scheme and a hybrid type limiter, which is the default standard model in CEDRE. The extrapolation to the interfaces was carried out on the natural variables. The temporal scheme was an explicit two-steps Runge-Kutta scheme, second order accurate. The time step was  $2 \mu\text{s}$  ( $\text{CFL} = 0.35$ ). As the sampling time step is  $4 \mu\text{s}$ , the results were stored every two iterations. The boundary conditions were a wall condition at the top, bottom and left sides of the cavity, and a constant pressure (1 bar) at the right side. At the initial instant, the cavity contained still air at ambient conditions, with the same pressure impulse described in sections 3.1, 3.2 and 3.3. However, the temperature inside the impulse pressure was adapted in order to make the impulse entropy at the initial instant equal to the entropy outside the impulse. These conditions are the most adapted to get results which are the closest to the theoretical solution. A parallel computation with 64 numerical sub-domains, on the same computer described in section 3.5, took less than 30 minutes to calculate the flow until 200 ms.

### 3.8 Preponderant modes detected by the DMD analysis

First, the CFD results were converted to 50 000 pressure files in a specific format used to read the data for the DMD analysis. This operation took about 3h 30mn on the same computer described in section 3.5.

Then, the DMD program, which works sequentially, required a size of 46.57 GB in the computer RAM and a CPU time of 47mn 04s to compute the amplitudes of 250 DMD modes below 1250 Hz. A specific time can be derived, with a view to estimate the CPU time of other modal amplitudes calculations, including files reading and writing :

$$t_{spec} = \frac{\text{CPU time}}{n_m \times n_s \times n_v} = \frac{2824 \text{ s}}{250 \times 50 \ 000 \times 125 \ 000} = 1.807 \ 10^{-9} \text{ s} \quad (3.7)$$

$n_m$  = number of considered modes ;

$n_s$  = snapshots number ;

$n_v$  = values number per snapshot.

The figure 3 shows the modal amplitudes of the pressure fluctuations at  $t = 0$ . Both cases are drawn, to highlight better the differences. Again, below 1250 Hz, 13 preponderant modes appear for the CFD flow, by visual observation of the amplitude peaks. The modes the peak of which is not high indicate a significant phase shift at  $t = 0$  (their maxima appear later during their own period). However, a frequency gap between the preponderant modes of the CFD flow and the ones of the theoretical solution appears, and increases with the modes frequency. The frequencies detected by the DMD analysis of the CFD results are written in the table 1.

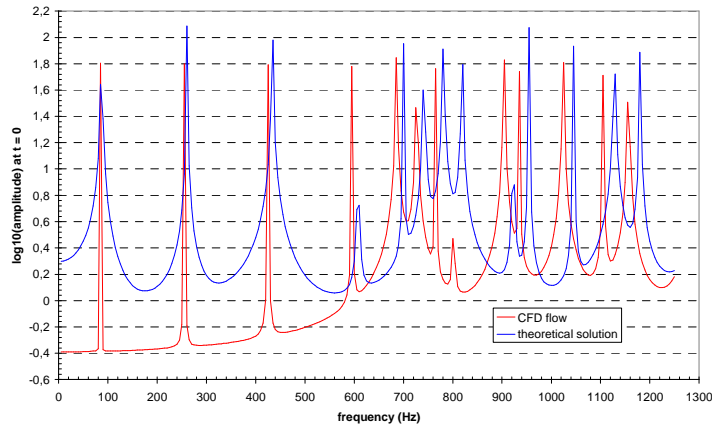


**Fig. 3.** Modal amplitudes of the validation case at  $t = 0$ .

If the gap between the DMD modes frequencies of the CFD flow and of the theoretical frequencies increases with the frequency, their relative differences remain roughly constant from the second longitudinal mode (about -2.1 %). These differences show the CFD flow is not the same as the ideal flow, from which the relation (3.2) derives. The code CEDRE is non linear, the CFD flow has a compressible nature, the mean velocity is not necessarily zero everywhere and the boundary conditions involve a special processing of the whole variables describing the flow. The theoretical frequencies are derived from linearized equations, assuming the mean flow incompressible and still, and the boundary conditions concern only the pressure and velocity fluctuations [15]. It is not the purpose of this paper to investigate further the issue.

### 3.9 Modal shapes of the CFD flow

The modals shapes of the CFD flow are presented in this paragraph (figures 4 and 5). The instants, extracted within the modes periods, are chosen in order to show the deformations at their maximum. The shapes are in good agreement with what is expected, with respect to the modal shapes of the theoretical solution.

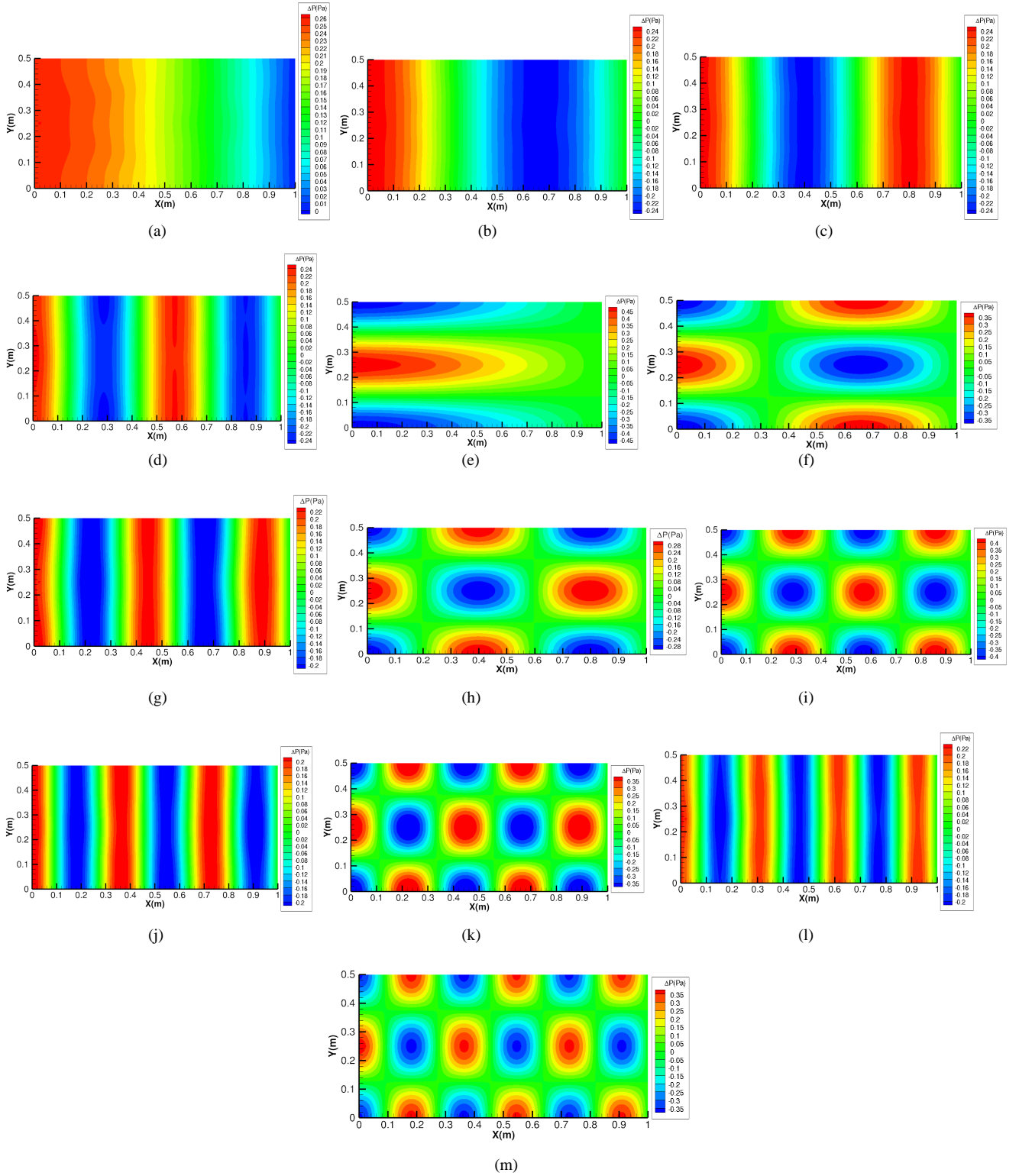


**Fig. 4.** (a)  $f = 85$  Hz, mode 1L,  $t = 11.752$  ms. (b)  $f = 255$  Hz, mode 2L,  $t = 3.908$  ms.  
(c)  $f = 425$  Hz, mode 3L,  $t = 2.340$  ms. (d)  $f = 595$  Hz, mode 4L,  $t = 1.664$  ms.  
(e)  $f = 685$  Hz, mode 2T,  $t = 1.332$  ms. (f)  $f = 725$  Hz, mode 2L-2T,  $t = 1.132$  ms.  
(g)  $f = 765$  Hz, mode 5L,  $t = 1.288$  ms. (h)  $f = 800$  Hz, mode 3L-2T,  $t = 0.948$  ms.  
(i)  $f = 905$  Hz, mode 4L-2T,  $t = 0.108$  ms. (j)  $f = 935$  Hz, mode 6L,  $t = 1.044$  ms.  
(k)  $f = 1025$  Hz, mode 5L-2T,  $t = 0.088$  ms. (l)  $f = 1105$  Hz, mode 7L,  $t = 0.876$  ms.  
(m)  $f = 1155$  Hz, mode 6L-2T,  $t = 0.720$  ms.

## 4. Application to a 3D CFD results case

### 4.1 Context

The geometry of the computational domain is the combustion chamber of the solid propellant engine LP6, the Ariane 5 P230 engine at a scale of 1/15 [19]. Some calculations were conducted to study the influence of the unstructured 3D mesh on the turbulence and on the acoustic response of the engine, with the aim to improve the understanding of the coupling between acoustics and instabilities generated by vortex-shedding caused by hydrodynamic instabilities [17, 20]. In the LP6 engine case, the identified mechanism of the hydrodynamic instabilities was the parietal vortex shedding (PVS), which results from a Taylor intrinsic instability of the internal flow when the mass flow comes from the lateral wall [22].

This DMD application focuses on the hydro-acoustic instabilities, and complements the acoustic studies which were already realized for the LP6 engine [20, 21].

### 4.2 Computational domain mesh and DMD analysis mesh

Three levels of non-structured mesh refinement were used to realize the calculations : a rough mesh of about  $2.5 \cdot 10^6$  cells, a mean mesh called GM of about  $19.6 \cdot 10^6$  cells, and a fine mesh called GF of about  $165.3 \cdot 10^6$  cells. The figure 5 shows the overall shape of the LP6 engine and a longitudinal section of the rough mesh in the plane  $z = 0$ . The coloured parts represent the propellant blocks.

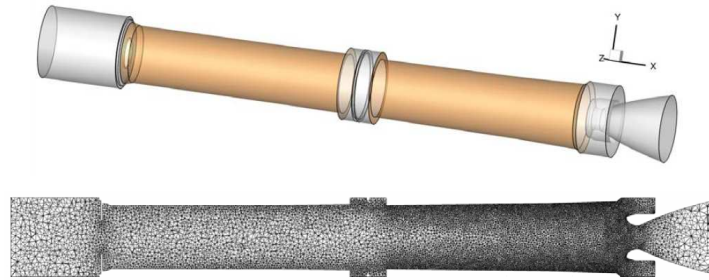


Fig. 5. Overall view of the LP6 engine.

As the instabilities were the most developed in front of the nozzle lips, a cloud of points was created in this area to store, in the course of the calculations, the pressure and the velocity field intended for some acoustic processing and modal analysis [20]. The figure 6 shows the location of this secondary mesh, which is used now for the DMD analysis. The points form a cylindrical ring with a rectangular section, the width of which is equal to about three quarters of the local chamber radius and the length is one and a half times the width. The secondary mesh is structured : 31 points in the axial direction, 31 points in the radial direction, and 301 points in the azimuth direction, making a total of  $31 \times 31 \times 301 = 289\,261$  values per snapshot.

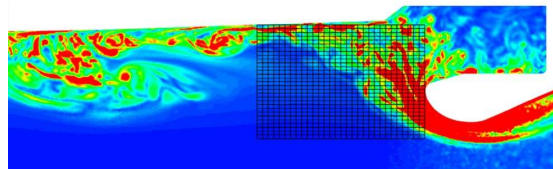


Fig. 6. Zoom in the plane  $z = 0$  of the rotational field with the mesh for the acoustic processing.

### 4.3 Conditions of the calculations

The 3D computations were performed with the finite-volume CFD code CEDRE [16, 17]. A single-phase approach was used with a Navier-Stokes solver, because the used propellant did not contain aluminium particles. The flow was non-reactive. The Euler fluxes were discretized using a HLLC scheme, with an intermediary state calculated by a Roe mean. The turbulence was simulated using a LES model, with a Smagorinsky subgrid model.

Two main calculations were performed [20]. The first one was second order accurate in space and in time with the GF mesh. The space interpolation on the natural variables was second order accurate, with no limitation function. The time integration scheme was implicit one step / one stage, with a coefficient  $\theta$  equal to 0.5, making the method

second order accurate. The linear system was solved using the GMRES method. The time step was  $0.2 \mu\text{s}$ . This scheme is twice faster than the RK2 scheme, and it is more robust in the case of very small tetrahedral cells, some of which can be awkward.

A second calculation, fourth order accurate in space and in time with the rougher GM mesh, was conducted with a higher order scheme to see whether the description of the instabilities would be improved. The space interpolation on the natural variables was fourth order accurate, with no limitation function. The time integration scheme was a Runge-Kutta four steps, fourth order accurate scheme. The time step was  $0.1 \mu\text{s}$ .

As the LP6 engine propellant response with respect to the pressure instabilities was not significant, the combustion of both propellant blocks was simply modelled by an injection boundary condition at constant flow rate and constant velocity combustion, with the same combustion temperature [20]. Inert surfaces were processed as adiabatic walls, and the nozzle exit as a supersonic exit.

Two sets pressure results, which were stored in both cases at the points of the secondary mesh, are available for a DMD analysis. They are named GF 2-order and GM 4-order in this paper, and both of them are submitted for a DMD analysis in a purpose of comparison. The mean pressure in the chamber was 41 bar. The sound velocity in the chamber, useful for further acoustic comparisons (see section 6.9), was 1059.87 m/s.

#### 4.4 Experimental results useful for the DMD analysis

Before the 3D calculations of the LP6 engine, several shots of this engine were fired in a test bench [18, 19, 23]. Some pressure measurements were collected. The reference values, which defined the calculations conditions, were derived from the measurements of the LP6 shot n° 7 at the instant 6.4 s of combustion. At the time of the tests, the experimental signals were filtered between 200 Hz and 2000 Hz [19]. Unfortunately, the presence of any mode beyond this band, which could be detected by the modal analysis or by the DMD analysis, is unknown. The figure 7 shows the pressures at the front face of the chamber, noted FAV, and at the rear face, noted FAR (within the annular space surrounding the nozzle convergent) [18, 20].

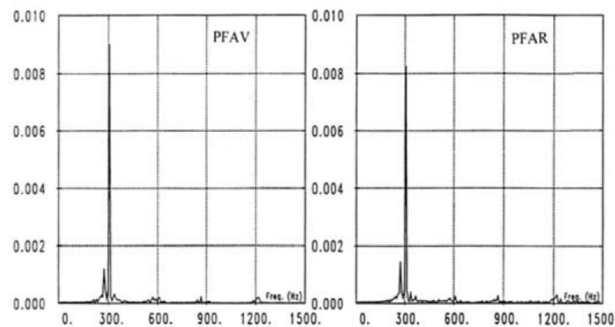
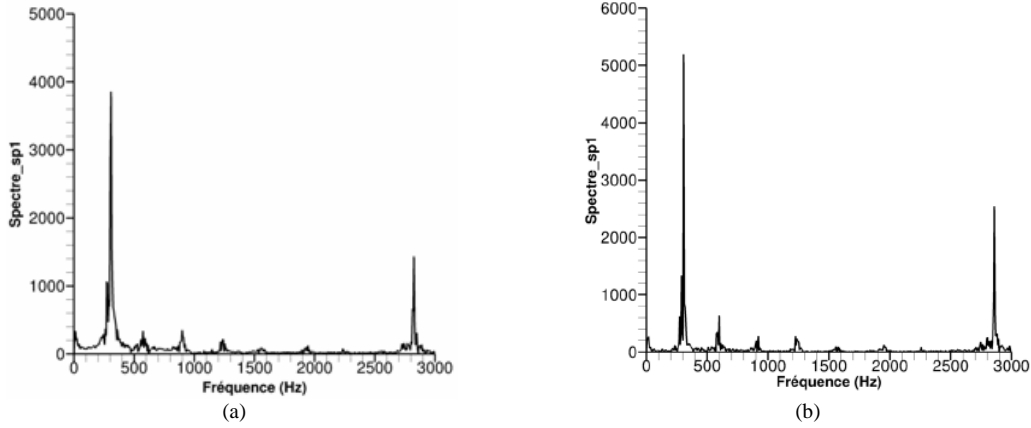


Fig. 7. Experimental FAV and FAR pressures (MPa).

A pressure peak appears around 300 Hz, which is likely the frequency of the first longitudinal acoustic mode. The peaks of the harmonic frequencies are very small.

#### 4.5 Modal analysis results

Regarding the modal analysis realized in 2017 and in 2018 through CFD results [20, 21], average values, RMS and DSP for the pressure and the velocity in the axial, radial and azimuth directions were calculated. For comparison purposes with the DMD analysis, since the acoustic study area is just in front of the nozzle, only the FAR pressures stored by sensors are considered. The figure 8 shows the time dependant evolutions of the FAR pressure for the GF 2-order calculation, and the GM 4-order calculation. In both cases, the resolution frequency was 6 Hz. Besides the main peak around 300 Hz and its harmonic frequencies, a second predominant peak appears around 2820 Hz for the GF 2-order calculation, and around 2850 Hz for the GM 4-order calculation. The table 2 gathers the frequencies of the first longitudinal mode, and the associated resolutions frequencies [20].



**Fig. 8.** FAR pressure (Pa) of the 3D GF 2-order calculation (a) and of the 3D GM 4-order calculation (b).

**Table 2**  
Acoustics modes frequencies in the 2D cavity.

	LP6 shot n° 7	3D GF 2-order	3D GM 4-order
1L frequency (Hz)	303	307	306
resolution frequency(Hz)	8	6	6

#### 4.6 Preponderant modes detected by the DMD analysis

For the GF 2-order calculation, 24300 snapshots were provided ( $N = 24299$ ), with a sampling time step of  $4 \mu\text{s}$ . Therefore the maximum detectable frequency is 125 kHz and the minimum resolution frequency is 10.288 Hz if all the snapshots are used.

For the GM 4-order calculation, 25500 snapshots were provided ( $N = 25499$ ), with a sampling time step of  $4 \mu\text{s}$ . Therefore the maximum detectable frequency is still 125 kHz and the minimum resolution frequency is 9.804 Hz if all the snapshots are used.

It would be tempting to use only 25000 snapshots of the GM 4-order case, which leads to the simple value of 10 Hz for the resolution frequency. Since the experimental pressure peak of the LP6 shot n° 7 is at 303 Hz, it is better to find a resolution frequency such as the peak frequency is the closest to a multiple of it. It is a way to check whether the first mode of the CFD flows, detected by DMD, matches the experimental one. If only 19802 snapshots are used ( $N = 19801$ ), the resolution frequency is equal to 12.625 Hz with a relative error of  $10^{-6}$ , and the experimental peak frequency is 24 times the resolution frequency. In addition, this number of snapshots is common to both cases, making more consistent a comparison between their DMD results. For the purpose of the study, the maximum observed frequency is limited to 5000 Hz.

While running the DMD program, a size of 42.69 GB in the RAM and a CPU time of 1h 07mn 55s were required to compute the amplitudes of 396 modes below 5000 Hz at  $t = 0$  in the GF 2-order case. A CPU time a little bit smaller (1h 03mn 48s) was required to compute the amplitudes of the same number of modes in the GM 4-order case. The specific time, defined by the relation (5.7), for the GF 2-order case is :

$$t_{spec} = \frac{\text{CPU time}}{n_m \times n_s \times n_v} = \frac{4075 \text{ s}}{396 \times 19\ 802 \times 289\ 261} = 1.797 \cdot 10^{-9} \text{ s} \quad (6.1)$$

The selection of the preponderant modes is made only by visual observation : the amplitude of a preponderant mode is higher than the amplitude of its neighbouring modes. The figure 9 shows the modal amplitudes of the pressure fluctuations at  $t = 0$  in the GF 2-order and GM 4-order cases. The main peaks are present in both cases at 303 Hz, its three following harmonics, and between 2800 Hz and 2900 Hz.

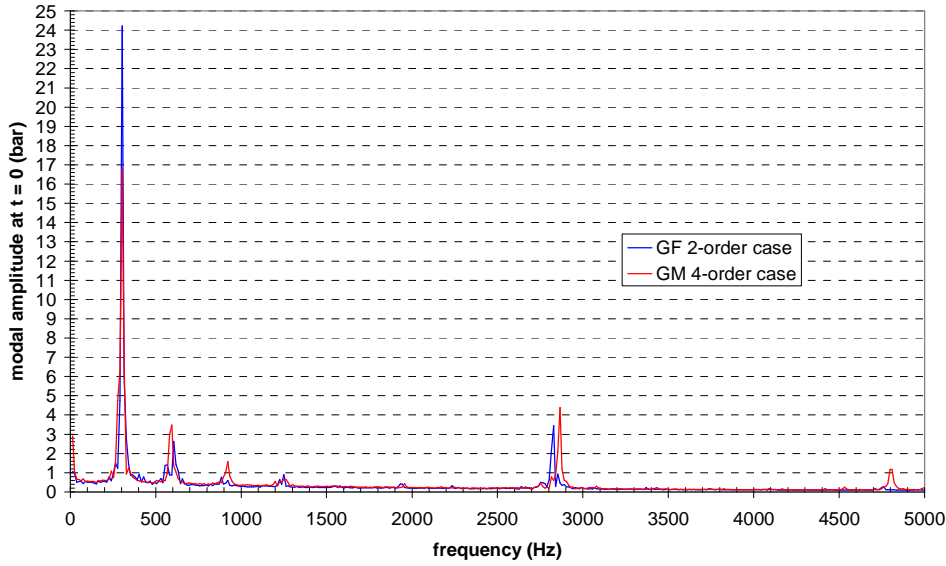


**Fig. 9.** Modal amplitudes in the GF 2-order and GM 4-order cases at  $t = 0$ .

If the modal frequencies are identical or very close for the first four preponderant modes, they are clearly distinct for the mode between 2800 Hz and 2900 Hz, and only the GM 4-order case shows another peak around 4800 Hz. The first peak is the highest in the GF 2-order case (24.22 bar against 16.76 bar in the GM 4-order case). The five following peaks are higher in the GM 4-order case, at least at  $t = 0$ . The selected frequencies in both cases are gathered in the table 3. For a matter of convenience, the values are rounded to the nearest unit.

Once a mode is selected, it is interesting to calculate the evolution of its amplitude over its whole period. In order to separate several modes next to each other, the amplitude of which is about the same at  $t = 0$ , but with a different evolution in the time. In order also to bring out the phase shifts between the modes, as mentioned in the section 2.7.

The highest mean value of the amplitudes among nearby modes over their own period decides which mode is the preponderant mode.

The figure 10 shows the time dependant evolution of the pressure fluctuations amplitudes of several modes over their own periods in the GF 2-order and GM 4-order cases. The curves are not sinusoidal. They bring out the modal amplitude and phase shift discrepancies due to the mesh and integration order differences.

**Table 3**  
Selected DMD frequencies.

GF 2-order case	GM 4-order case
303 Hz	303 Hz
	581 Hz
	593 Hz
606 Hz	606 Hz
884 Hz	
922 Hz	922 Hz
1225 Hz	
1237 Hz	
1250 Hz	1250 Hz
	1263 Hz
2828 Hz	2866 Hz
	4798 Hz
	4810 Hz



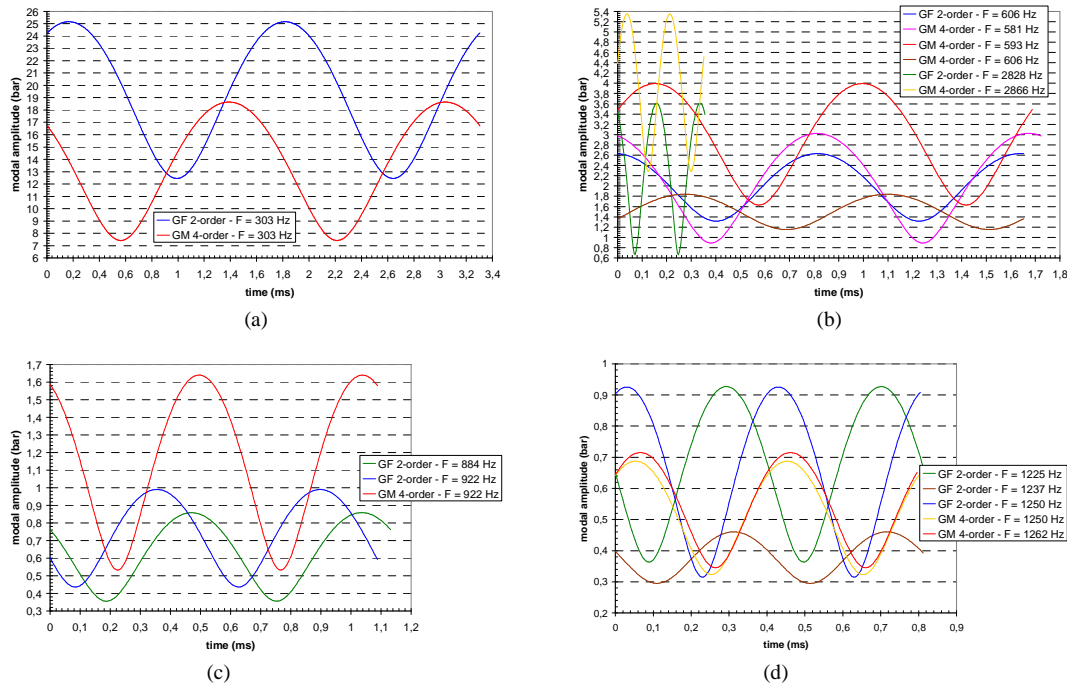


**Fig. 10.** Time dependant evolution of the amplitude of the modes at 303 Hz (a), around 600 Hz, and between 2800 Hz and 2900 Hz (b), around 900 Hz (c), and around 1250 Hz (d), over their own period.

The graph (a) concerns the first mode at 303 Hz, and shows clearly the GF 2-order case fits to describe the shape evolution, since the mode amplitude is higher.

The graph (b) concerns the modes around 600 Hz, and between 2800 Hz and 2900 Hz. In a pure acoustic configuration, the first harmonic of the mode at 303 Hz is normally at 606 Hz. The GF 2-order case brings it out. In the GM 4-order case, it is covered by two other modes at lower frequencies, and the most preponderant mode in that case is clearly at 593 Hz. The phase shifts of the modes, the frequencies of which are nearby, vary in the end a lot according to the case and the frequency. The preponderant mode between 2800 Hz and 2900 Hz is tangential (see figure 15). The GF 2-order case gives a frequency at 2828 Hz while the GM 4-order case gives a frequency at 2866 Hz with a higher amplitude.

The graph (c) concerns the modes around 900 Hz. The curves in the GF 2-order case are an example where the mode at 884 Hz seems to be preponderant at  $t = 0$  compared to the mode at 922 Hz. Over their own period, the mode at 922 Hz has a higher mean value than the mode at 884 Hz. That mode is even more preponderant in the GM 4-order case.

In the end, the graph (d) concerns the modes around 1250 Hz. Because of several ambiguities at  $t = 0$ , several curves are plotted. The highest mean value of the modes amplitudes over their own period is at 1250 Hz in the GF 2-order case. The curves of the modes around 4800 Hz in the GM 4-order case are not plotted. The mean value of the mode at 4798 Hz is the highest.

#### 4.7 Comments

Plotting the modal amplitudes in the time helps to determine which modes are preponderant according to the case (GF 2-order or GM 4-order). But once the preponderant modes are found, there is no way to say what case is better than the other to explain the physics. Only some experimental measurements can help to decide. As it can be suspected, the influence of the mesh and integration scheme on the DMD results is eventually quite important.

#### 4.8 Time dependant evolution of the modal shapes

A great advantage of the DMD is the possibility to show the time dependant evolution of the shapes of the selected preponderant modes. The modal shapes are the fluctuations shapes calculated with respect to the rigid mode.

For each mode, some slides at various moments are extracted from a video which runs over one period of the mode. Only the modes which present the highest peaks are considered in this paragraph. To give an idea of what happens within the numerical domain intended to the modal analysis, a quarter of the cylindrical secondary mesh is

removed, revealing a vertical plan, a horizontal plan, and the inner cylindrical surface of the mesh. The plan which sticks to the nozzle nose is in front. Since the modal shapes are here the pressure fluctuations shapes, this explains why the term  $\Delta P$  in the legend is used, and why the amplitude of  $\Delta P$  is positive or negative. The extreme values of  $\Delta P$  are significantly reduced compared to the real extreme values of a modal shape, in order to highlight better the visible phenomena.

The figure 11 shows the shapes of the mode at 303 Hz in the GF 2-order case ( $\Delta P_{extreme} = \pm 10^4$  Pa). Nine moments are selected (beginning and every next 8<sup>th</sup> period) to show properly the evolution. The mode is affected by an important radial influence. The pressure variations come from the outside to the inside of the domain, and close to the nozzle. Hence the annular cavity around the nozzle convergent has an important influence on this mode.

The figure 12 shows the shapes of the mode at 593 Hz in the GM 4-order case ( $\Delta P_{extreme} = \pm 1200$  Pa). Three moments are selected : both maxima of amplitude, separated by the first minimum of amplitude. The shape evolution of this mode is more classical for a longitudinal mode, with still a significant influence of the nozzle edge.

Both modes at 922 Hz (case GM 4-order, figure 13,  $\Delta P_{extreme} = \pm 600$  Pa) and at 1250 Hz (case GF 2-order, figure 14,  $\Delta P_{extreme} = \pm 400$  Pa) show a quite important influence of the nozzle edge and the annular cavity around the nozzle convergent on the shape evolution, without any significant longitudinal pressure variation.

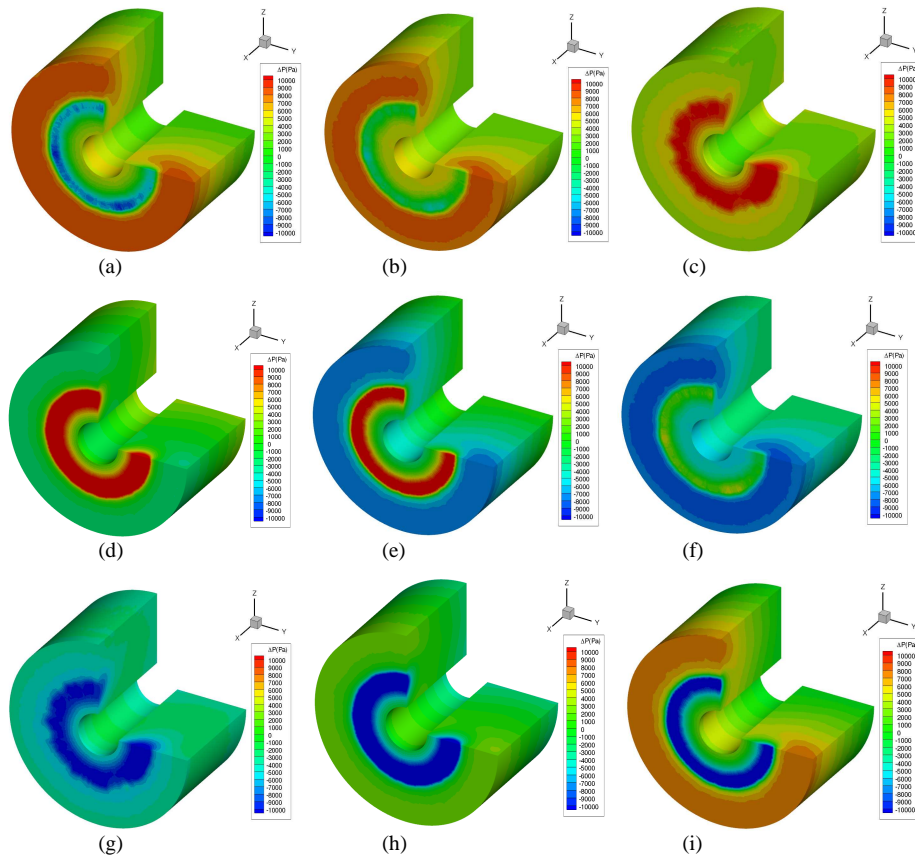


**Fig. 11.** Shapes of the mode at 303 Hz in the GF 2-order case, at  $t = 0$  (a),  $t = 168 \mu\text{s}$  (b),  $t = 580 \mu\text{s}$  (c),  $t = 992 \mu\text{s}$  (d),  $t = 1404 \mu\text{s}$  (e),  $t = 1816 \mu\text{s}$  (f),  $t = 2228 \mu\text{s}$  (g),  $t = 2640 \mu\text{s}$  (h),  $t = 3052 \mu\text{s}$  (i).

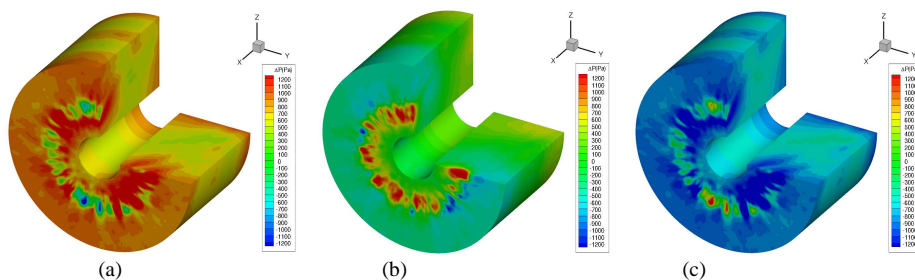


**Fig. 12.** Shapes of the mode at 593 Hz in the GM 4-order case, at  $t = 152 \mu\text{s}$  (a),  $t = 576 \mu\text{s}$  (b),  $t = 996 \mu\text{s}$  (c).

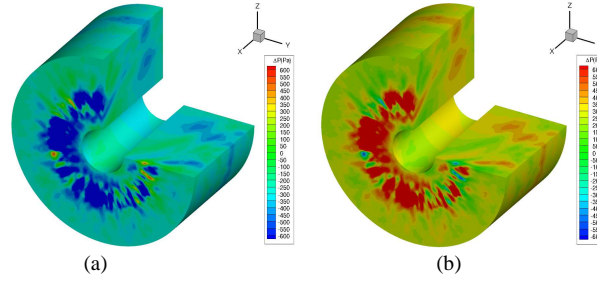


**Fig. 13.** Shapes of the mode at 922 Hz in the GM 4-order case, at  $t = 496 \mu\text{s}$  (a),  $t = 1040 \mu\text{s}$  (b).

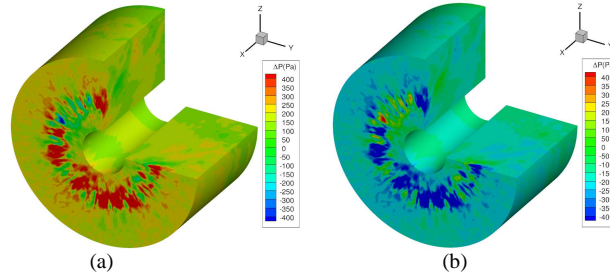


**Fig. 14.** Shapes of the mode at 1250 Hz in the GF 2-order case, at  $t = 28 \mu\text{s}$  (a),  $t = 428 \mu\text{s}$  (b).

The next mode at 2866 Hz in the GM 4-order case, second preponderant mode after the one at 303 Hz, is the first pure tangential mode, the shape of which rotates clockwise at the frequency of the mode, while it oscillates between its two extrema. The nine selected moments (figures 16,  $\Delta P_{\text{extreme}} = \pm 2500 \text{ Pa}$ ), show the shape evolution of this mode, starting from  $t = 0$ , then every next 8<sup>th</sup> period to highlight the rotation.

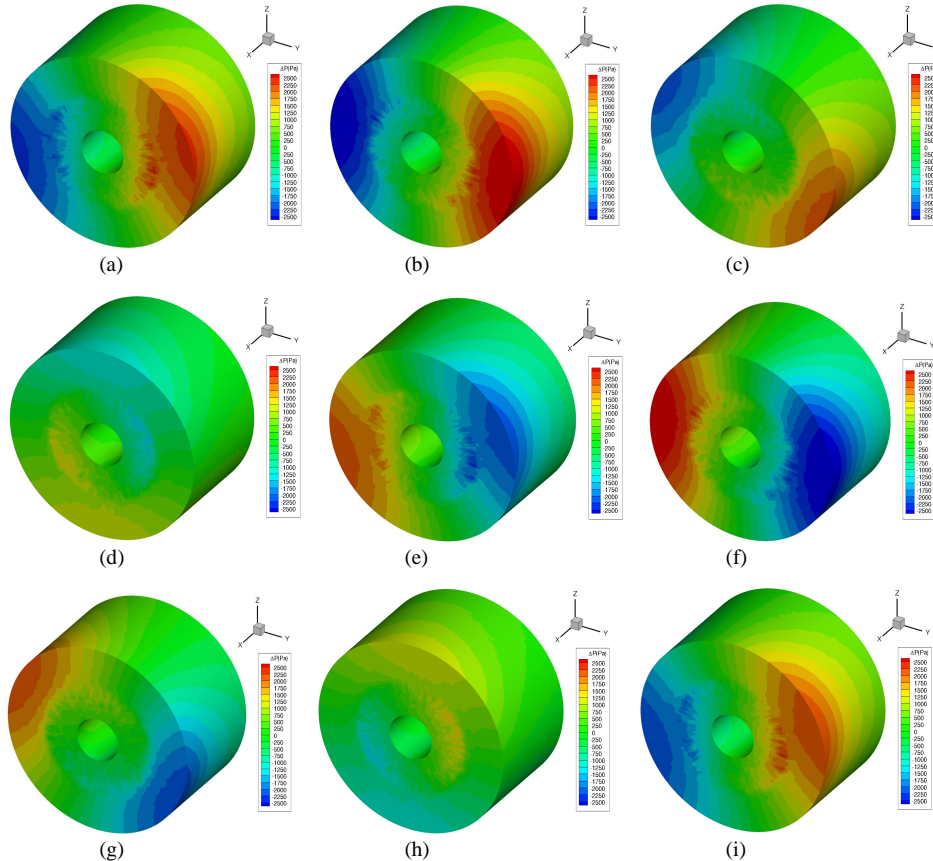


**Fig. 15.** Shapes of the mode at 2865.875 Hz in the GM 4-order case, at  $t = 0$  (a),  $t = 40 \mu\text{s}$  (b),  $t = 84 \mu\text{s}$  (c),  $t = 124 \mu\text{s}$  (d),  $t = 168 \mu\text{s}$  (e),  $t = 212 \mu\text{s}$  (f),  $t = 256 \mu\text{s}$  (g),  $t = 300 \mu\text{s}$  (h),  $t = 344 \mu\text{s}$  (i).

The last mode at 4798 Hz, in the GM 4-order case, is also interesting since it seems to be the second pure tangential mode. The mode shape rotates clockwise. The eight selected moments (figure 17,  $\Delta P_{extreme} = \pm 800$  Pa), show the shape evolution of this mode, starting from the first maximum at 8  $\mu$ s, then every next 8<sup>th</sup> period to highlight the rotation.

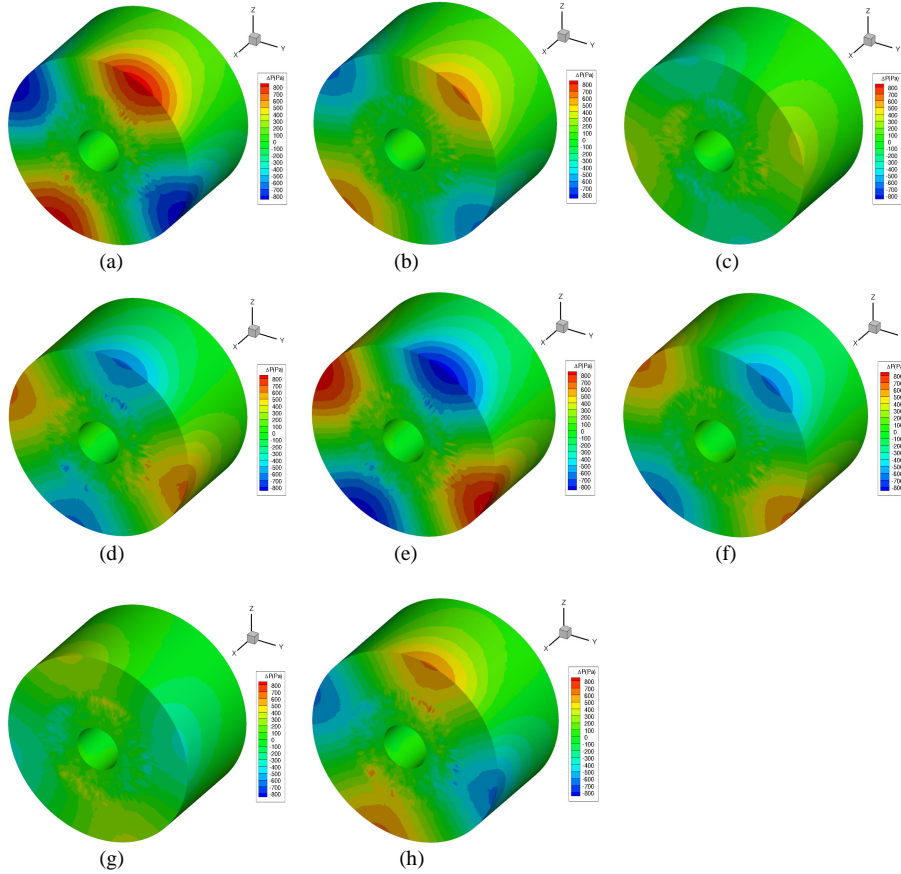


**Fig. 16.** Shapes of the mode at 4798 Hz in the GM 4-order case, at  $t = 8 \mu$ s (a),  $t = 36 \mu$ s (b),  $t = 60 \mu$ s (c),  $t = 84 \mu$ s (d),  $t = 112 \mu$ s (e),  $t = 140 \mu$ s (f),  $t = 164 \mu$ s (g),  $t = 188 \mu$ s (h).

#### 4.9 Comparison with the pure acoustic modes

The first preponderant mode detected by the DMD analysis derives in principle from a coupling between the chamber acoustics and the PVS instability. To know exactly the acoustic modes of the LP6 engine, and thus to estimate the influence of the coupling, the AVSP software, made by CERFACS, was used in the whole domain of the chamber. As this software requires a small fluid velocity, the nozzle convergent was truncated at a position between the nose and the throat, which seems to be a good compromise between the respect of the engine geometry until the throat, and the necessity to remove the cells where the fluid velocity is too high and would lead to some wrong results if they were taken into account. The first hundred acoustic modes were computed. Only the modes which are close to the DMD modes are kept. As the parameters (pressure, temperature and molar mass of the gases) asked by AVSP to calculate the sound velocity give a value (1088.13 m/s) slightly different from the real value (1059.87 m/s) provided by the CFD calculation, a last correction was made on the AVSP frequencies values (through the sound velocity values ratio) to be consistent with the thermodynamic state of the LP6 engine. The table 4 gathers the AVSP and DMD modal frequencies. The adjusted AVSP frequencies are slightly smaller below 1000 Hz than the retained DMD frequencies, and slightly higher above 2000 Hz. Here, the values are rounded to the second decimal, to let appear some frequencies which are in pairs very close to each other, according to AVSP, for both pure tangential modes. This is the way used by the software to detect the tangential rotation of these modes. The figures 17 and 18 show the AVSP modes shapes, in order to determine the type of each mode. As a reduced absolute pressure is plotted, both maxima and minima in red and blue colours in the previous figures (11 to 16) become maxima plotted in red. Thus the blue colour represents the pressure knots.

**Table 4**  
AVSP and DMD modal frequencies.

$f_{AVSP}$ (Hz)	type	$f_{AVSP}$ (Hz) adjusted	$f_{DMD}$ (Hz) GF 2-order	$f_{DMD}$ (Hz) GM 4-order	dF / F (%)
306.7	1 L	298.77	303	303	-1.4
604.15	2 L	588.46	606	593.37	-0.83
937.53	3 L	913.18	921.62	921.62	-0.92
1283.47	4 L	1250.14	1249.87	1262.5	-0.98
2948.86	1 T	2872.27	2828	2865.87	0.22
2948.87	1 T	2872.28	2828	2865.87	0.22
4936.63	2 T	4808.42	-	4797.5	0.23
4936.76	2 T	4808.55	-	4797.5	0.23

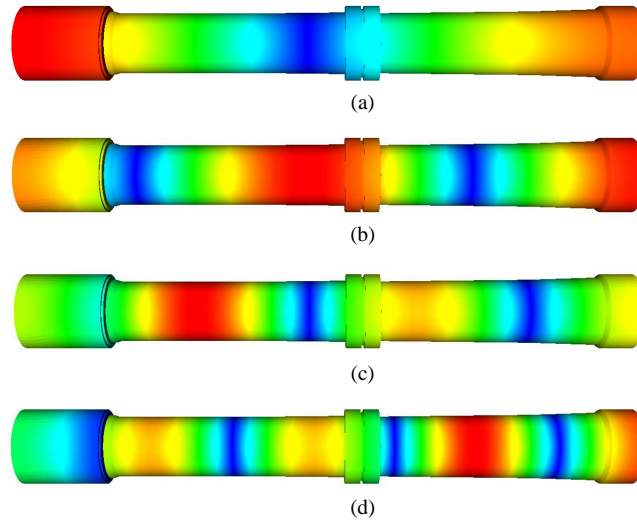


**Fig. 17.** AVSP modes, 1L (a), 2L (b), 3L (c), 4L (d).

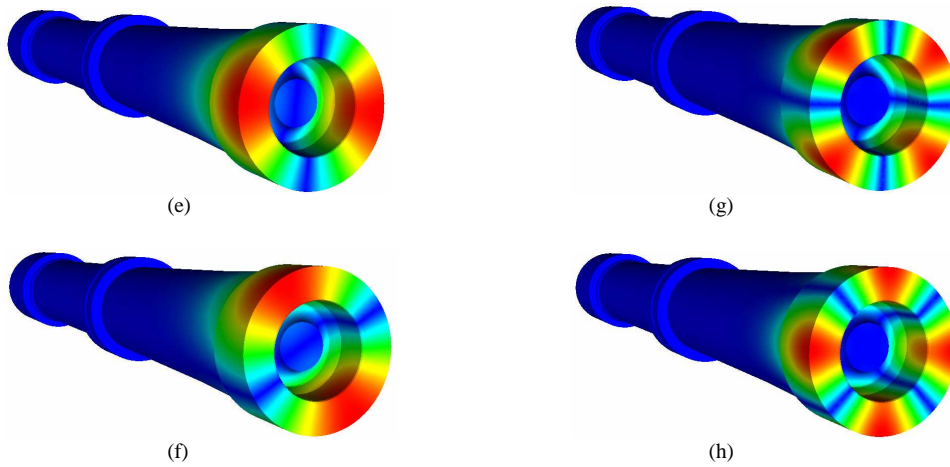


**Fig. 18.** AVSP modes, 1T (e) & (f), 2T (g) & (h).



#### 4.10 Comments on the 1L and 1T DMD modes

Since the peak at 303 Hz is the highest (figure 9), it means the coupling between acoustics and the PVS instability is strong. The frequency of one of the PVS modes of the LP6 chamber might be close enough to the first acoustic mode to merge with it and produce the high amplitude peak of the resulting DMD mode. With such a high amplitude, compared with the other DMD peaks, the PVS mode in question might be also unstable, in such a way that the acoustics and PVS instabilities amplify each other. It is not the purpose of this paper to investigate further the issue.

The second highest peak on the figure 9 corresponds to a tangential rotating mode in the cavity around the nozzle (figures 16 and 19). The frequency of this DMD mode in the GM 4-order case (2865.87 Hz) is quite close to the adjusted frequency of the 1T pure acoustic mode (2872.27 Hz). Therefore another coupling between acoustics and another phenomenon, which is unknown, might be important. A peak about the same frequency appears in the FAR pressure graphs of the 3D calculations (figure 8). Unfortunately, whether the peak would appear in the experimental measurements remains unknown, since the signals frequencies were cut above 2000 Hz [19].

However, it is possible that this mode is caused by a pure numerical effect. In a CFD calculation, the walls are perfectly impermeable and reflective. In addition, the LP6 calculations were conducted without any thermal transfer along the walls. Hence a small numerical instability generated close to the 1T mode frequency is likely to be amplified. In the real LP6 engine, the propellant is porous, and absorbs partially the acoustic energy. The parietal heat losses behave the same way. Therefore a small instability generated close to the 1T mode frequency is more likely to be damped in the working real chamber.

### 5. Application to two experimental films

#### 5.1 Context

In the framework of CNES-ONERA R&D activities for a rocket engine, a test campaign was run on the Mascotte test facility of ONERA, to characterize the atomization process and the combustion regimes, and to supply a database for validation of models and numerical simulation tools.

For a matter of confidentiality, no reference is mentioned in this paper about these activities, the results of which are used for DMD only to present an interesting application case with experimental data.

The main purpose of the test series, from the point of view of optical diagnostics, was to film the flame using two high-speed cameras which were spatially adjusted (same field viewed by both cameras) and synchronized (images recorded at the same time). A first camera recorded the chemiluminescence of the OH\* radicals, which is correlated with the temperature, via an image intensifier. The second camera was used to visualize the liquid phase by shadow imaging. Both cameras had  $1280 \times 800$  pixels, with a resolution of 13 pixel/mm. The rough images were cut to the format  $1024 \times 512$  pixels before being recorded.

A shot was selected for the DMD analysis. The films showed a phenomenon of jets and flame pulsation. For this shot, the sampling frequency was 7400 Hz. A narrow band filter was mounted on the UV lens of the OH\* camera.

#### 5.2 Experimental results useful for the DMD analysis

A detailed frequency analysis was made for both films of the selected shot. For all the following images, the fluids move from the left (injectors plane) to the right (downstream). The mean and RMS images were calculated with 5000 images during the steady part of the flow (figure 19 for the OH\* radicals images, figure 20 for the shadow images). The projected shadow of the liquid phase is recorded on the retro-lighting images. The figure 20 shows two unsteady OH\* radicals images. The diffuse fluid near the injection takes place around the flame from the injector exit. Sometimes, the flame seems to close before the end of the viewing area and shows some puffs. No Abel transform was calculated, because of its questionable physical validity as digital tomography, due to the masking effect of the diffuse fluid.

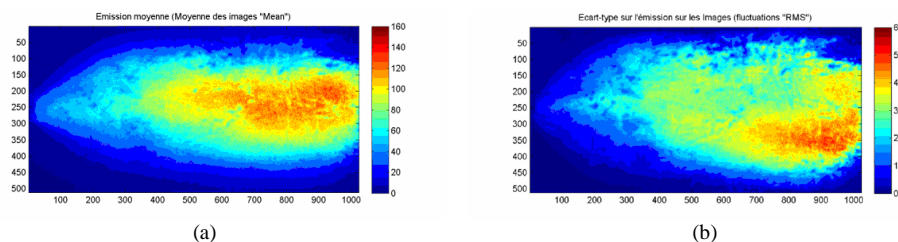
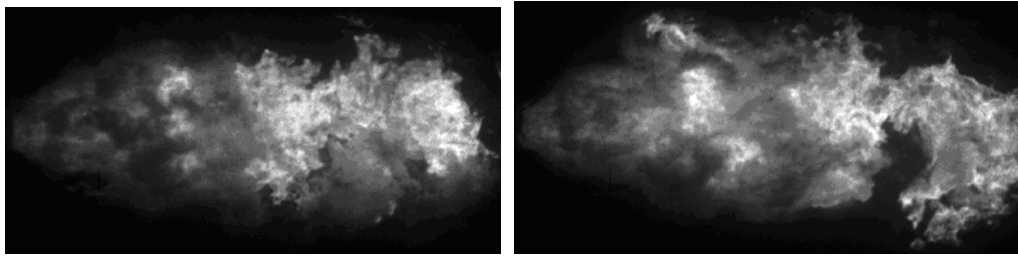
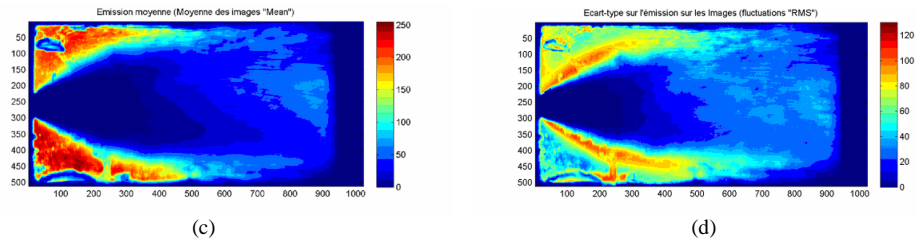


Fig. 19. Mean (a) and RMS (b) OH\* images with the narrow band filter.



**Fig. 20.** Unsteady OH\* radicals images.



**Fig. 21.** Mean (c) and RMS (d) shadow images.

A first global Fourier analysis was made on the OH\* radicals images. Each of them being beforehand spatially averaged, the spectral power density (SPD) of the time dependant resulting signal was then calculated (figure 22). A main peak appears around 2500 Hz. A second very small peak around 3100 Hz seems to come out of the noise.

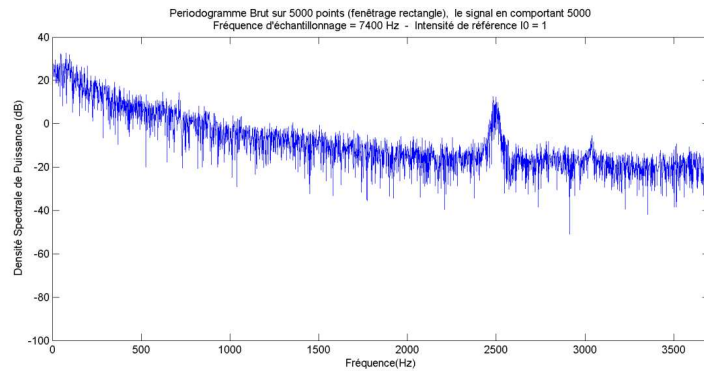


**Fig. 22.** SPD of the averaged OH\* radicals images.

The Fourier treatment was then focused on six parts of equal surface in the viewing area. Two other SPD examples, one for the OH\* radicals images in a part of the viewing area, and one for the shadow images in another part, are displayed on the figure 23. In both cases, the obtained SPD shows a little peak at exactly 865 Hz. The peak near 2500 Hz appears only for the OH\* images.

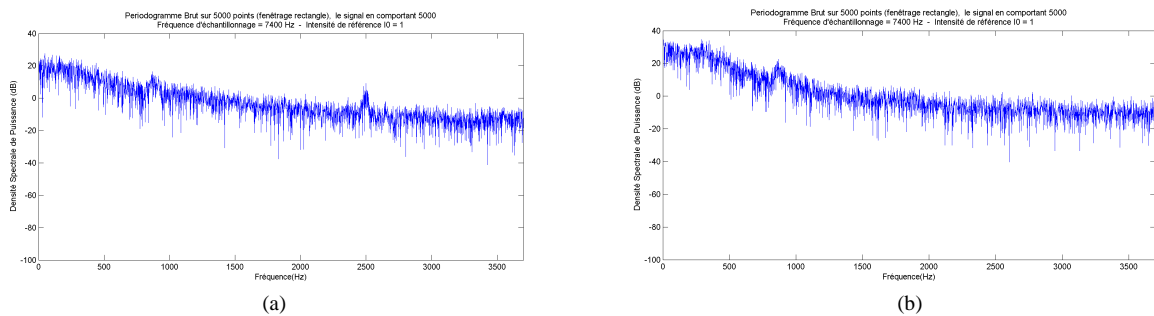


**Fig. 23.** SPD examples of the OH\* radicals images (a), and the shadow images (b) in parts of the viewing area.

### 5.3 Preponderant modes detected by the DMD analysis for the OH\* radicals film

The OH\* radicals film was composed of 16001 images (at most  $N = 16000$ ), with a sampling frequency of 7400 Hz. Hence the maximum detectable frequency is 3700 Hz and the minimum resolution frequency is 0.4625 Hz, which is very low. Each image has 1024 pixels in abscissa and 512 pixels in ordinate, which makes a total of 524 288 values per snapshot, with a spatial resolution of 13 pixel / mm.

While running the DMD program, a size of 62.57 Go in the RAM and a total CPU time of 27h 55mn 48s were required to compute the amplitudes of 8000 modes below 3700 Hz at  $t = 0$ . The specific time, calculated with the relation (3.7), is  $1.498 \cdot 10^{-9}$  s. The part (a) of the figure 24 shows the modal amplitudes at  $t = 0$  of the fluctuations of the pixels grey levels, calculated with all the snapshots, over the whole frequency domain.

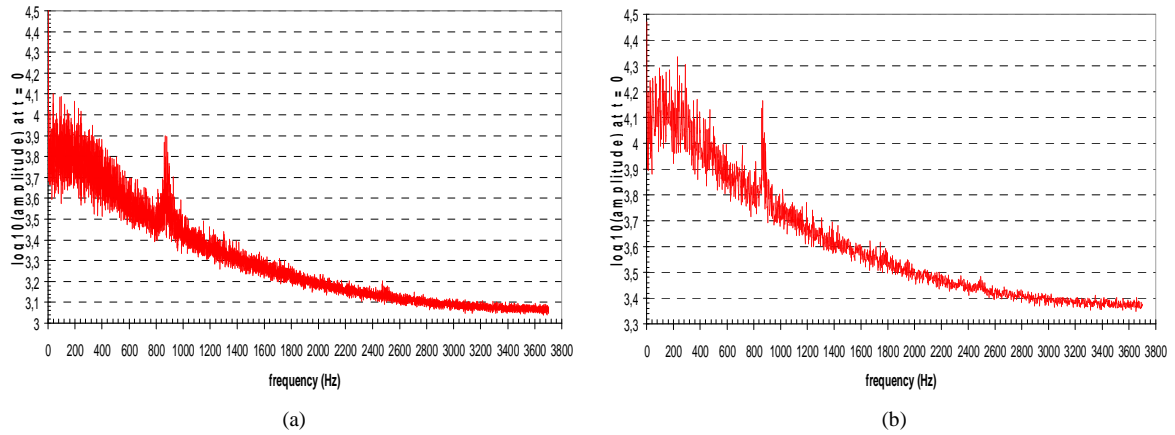


**Fig. 24.** Modal amplitudes for the OH\* radicals film at  $t = 0$ , for  $N = 16000$  (a), and for  $N = 3699$  (b).

The selection of the preponderant modes is made only by visual observation : the amplitude of a preponderant mode is higher than the amplitude of its neighbouring modes. In the case of a DMD analysis from experimental data, the preponderant modes seem to appear like a « bell », in opposition to CFD data where the preponderant modes are very clear at a single frequency. The high value of the sampling time step (near 135  $\mu$ s), much higher than the time step in the CFD case (4  $\mu$ s), may explain this behaviour, since it leads, with all the snapshots, to a very low resolution frequency. If this frequency is too small, it is then possible that several modes, which provide a similar shape, are captured by several very close frequencies. The amplitude of the phenomenon is then distributed on each of the nearby modes, and it is then difficult to determine a single value of the preponderant mode frequency. If the experimental data comes from an exciting source at a given frequency, then the behaviour associated to the CFD for the DMD analysis is likely to be found again. In this experimental case, the spectrum noise is also quite important, since the images are not filtered.

The figure 24 shows the main phenomenon appears between 850 Hz and 900 Hz. To increase the resolution frequency with a fixed sampling frequency, and therefore, to highlight the preponderant modes at distinct frequencies, it is then required to dim the snapshots number. Then the preponderant mode can be selected more easily. In addition, it is more convenient to choose a snapshots number such as the resolution frequency has a simple value. For the OH\* radicals, 3700 snapshots are used (taken here from the 4000<sup>th</sup> snapshot), and the resolution frequency is 2 Hz.

The part (b) of the figure 24 shows the new modal amplitudes at  $t = 0$  of the fluctuations of the pixels grey levels. The modal amplitudes as a whole for a reduced number of snapshots are higher than in the case with all the snapshots. Since the sum of all the modal vectors is always equal to the first snapshot regardless of the snapshots number (relation (2.33) with  $j = 0$ ), it is reasonable to admit, though it is not proved in this paper, that an increasing snapshots number leads overall to a lower amplitude for each modal vector. Four frequencies are selected : 230 Hz, 288 Hz, 866 Hz and 2494 Hz. The preponderant DMD mode in the OH\* radicals film appears at 866 Hz ( $\pm 1$  Hz).

### 5.4 Time dependant evolution of the modal shapes for the OH\* radicals film

For each selected frequency, a video showing the time dependant evolution of the mode shape can be built. But the modal shapes in this paragraph are shown only at the initial instant (figure 25), because the shapes at further instants do not bring much information. Since the modal shapes are the fluctuations shapes calculated with respect to the



rigid mode, the amplitude is positive or negative. The extreme values are reduced compared to the real extreme values of the shapes, in order to highlight better the visible phenomena.

The shapes evolutions of the two modes with a high peak at a low frequency (230 Hz and 288 Hz), show a pulsation phenomenon which grows approximately in the middle of the viewing area and moves downstream. It seems to follow the puffing phenomenon of the flame, mentioned in the section 5.2.

For the main mode at 866 Hz, the pulsation phenomenon grows from the injection plane before moving downstream and stretching to the upper and lower sides. The waves of the jet mixing zone look conical until about the first third of the viewing area, then they move downstream more longitudinally before they vanish. Since the amplitudes are maximum in the middle of the images, a wavelength  $\lambda$  was measured, along an axial line at  $y = 0.2$  m and around the abscissa  $x = 0.4$  m. It was found  $\lambda = 160$  mm (approximately). A phase velocity can be derived, as the product of  $\lambda$  by the frequency. It is equal to 138.56 m/s. This mode has nothing to do with the acoustics of the chamber, whose first longitudinal mode was calculated at about 611 Hz.

The mode at 2494 Hz shows some narrow and swift waves, which take place in the downstream half of the viewing area and which are rather longitudinal.

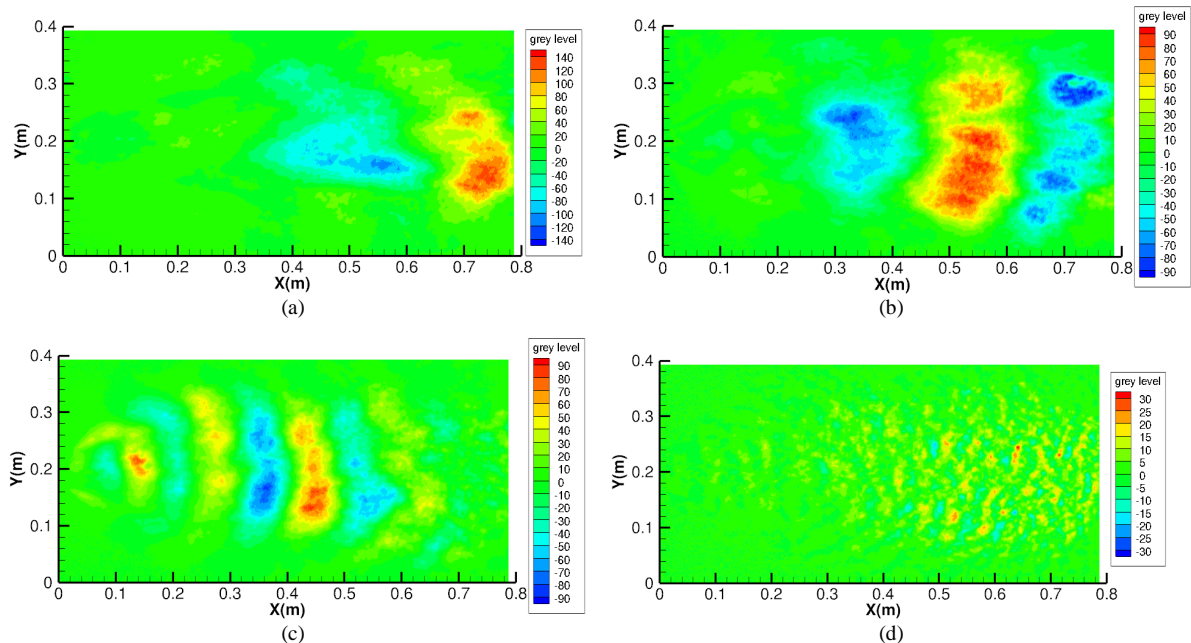


Fig. 25. Modal shapes at  $t = 0$  for the OH\* radicals.  $f = 230$  Hz (a),  $f = 288$  Hz (b),  $f = 866$  Hz (c),  $f = 2494$  Hz (d).

### 5.5 Preponderant modes detected by the DMD analysis for the shadow imaging film

The shadow imaging film was composed of 12281 images (at most  $N = 12280$ ), with a sampling frequency of 7400 Hz. The maximum detectable frequency is still 3700 Hz and the minimum resolution frequency is 0.6025 Hz, which is still very low. Each image has still 1024 pixels in abscissa and 512 pixel in ordinate, which makes a total of 524 288 values per snapshot, with a spatial resolution of 13 pixel / mm.

While running the DMD program, a size of 48.02 Go in the RAM and a total CPU time of 15h 47mn 48s were required to compute the amplitudes of 6140 modes below 3700 Hz at  $t = 0$  (the calculations was split up into two parts to respect the maximum allowed CPU time). The specific time, calculated with the relation (5.7), is here equal to  $1.438 \cdot 10^{-9}$  s.

The part (a) of the figure 26 shows the modal amplitudes at  $t = 0$  of the fluctuations of the pixels grey levels, calculated with all the snapshots, over the whole frequency domain.

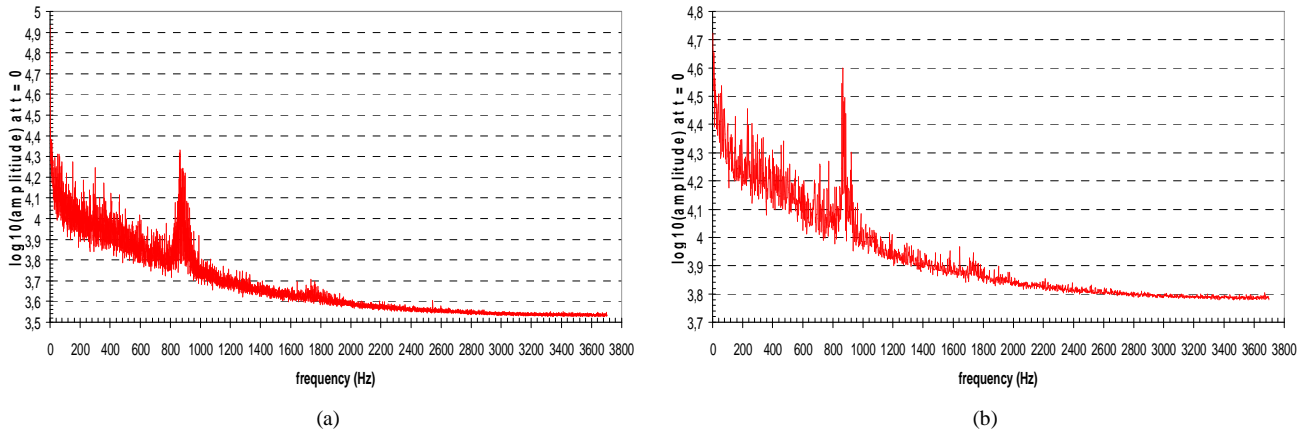


Fig. 26. Modal amplitudes for the shadow images at  $t = 0$ , for  $N = 12280$  (a), and for  $N = 3699$  (b).

Again, the preponderant modes seem to appear like a « bell », and the main phenomenon appears between 850 Hz and 900 Hz. The resolution frequency must be increased, to highlight the predominant modes at distinct frequencies. Since the sampling frequency is fixed, the number of snapshots must be reduced. For the shadow images, it is better to use again 3700 snapshots (taken here from the 4000<sup>th</sup> snapshot) than all them, and the resolution frequency is again 2 Hz. From the part (b) of the figure 26, three modes are selected : 230 Hz, 866 Hz and 1734 Hz. The preponderant DMD mode in the shadow imaging film appears again at 866 Hz ( $\pm 1$  Hz).

### 5.6 Time dependant evolution of the modal shapes for the shadow imaging film

The time dependant evolution of the selected modes shapes is presented in this paragraph. For each mode, some slides at various moments are extracted from a video which runs over one period of the mode. The shape evolution of the mode at 230 Hz is shown about every next quarter period (figure 27). The time dependant shapes show clearly the separation between the mixing zone of the jet and the recirculation zone between the injector and the walls. The strongest deformations take place along the border around the mixing and burning zone, where the non homogeneities between gas and liquid are the most important.

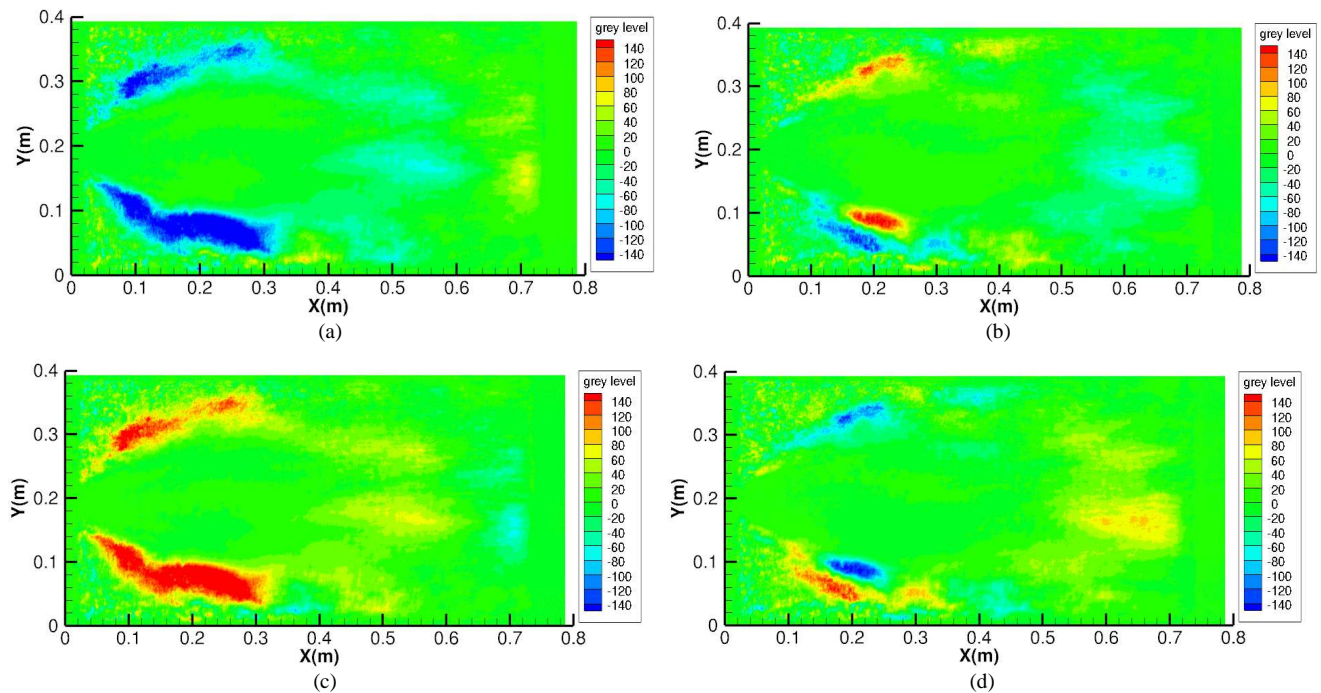
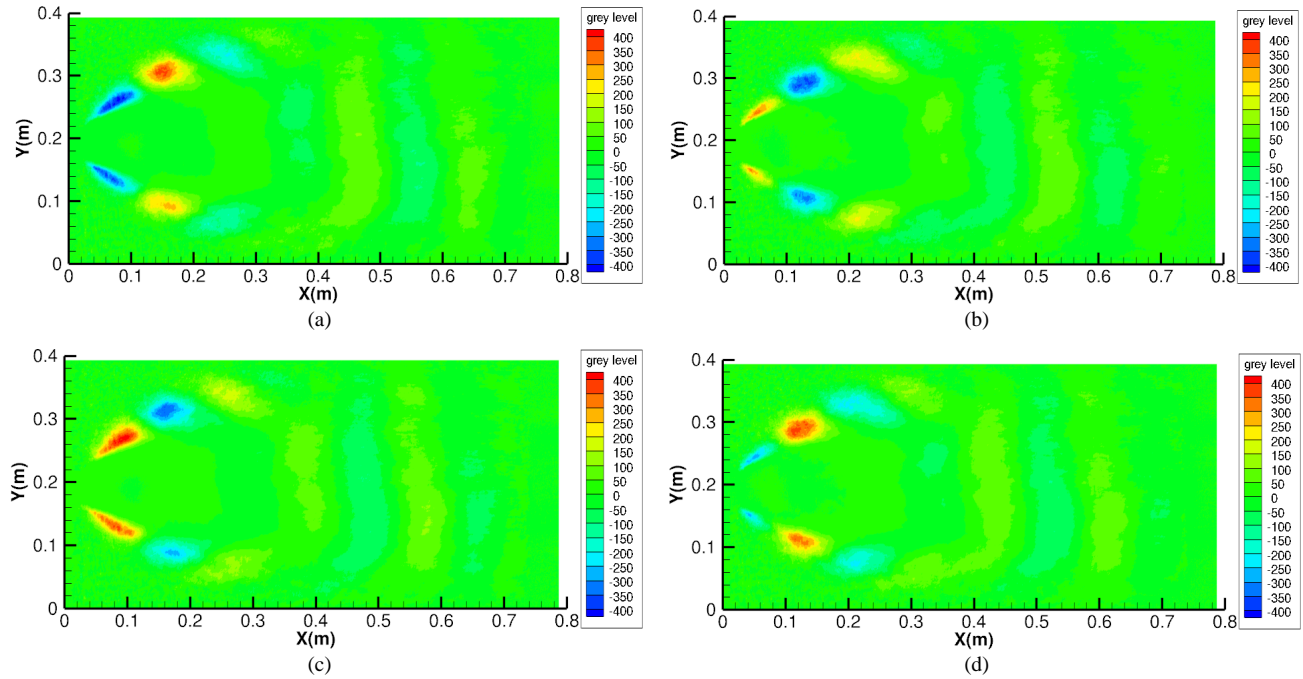


Fig. 27. Shapes of the mode at 230 Hz for the shadow images, at  $t = 270 \mu s$  (a),  $t = 1351 \mu s$  (b),  $t = 2432 \mu s$  (c),  $t = 3514 \mu s$  (d).

The most interesting mode is at 866 Hz. Four moments are shown, from the beginning and every next quarter period (figure 28). These images complement the images of the OH\* radicals pulsations at the same frequency. The pulsations occur essentially along the separation cone between the mixing zone of the jet and the recirculation zone between the injector and the walls. The contrast between liquid and gaseous phases seems to be maximal along this surface, for the considered frequency. It is therefore easy to measure a wavelength, estimated at 196.25 mm, as well as the angle of opening of the friction cone, estimated at  $31.67^\circ$ . The phase velocity in this direction is then equal to 169.95 m/s. The mode at 1734 Hz seems to be the first harmonic of the previous mode (figure 29).

Investigating further the issue about the atomization process, in particular for the preponderant mode, goes beyond the purpose of this paper.



**Fig. 28.** Shapes of the mode at 866 Hz for the shadow images, at  $t = 0$  (a),  $t = 405 \mu\text{s}$  (b),  $t = 676 \mu\text{s}$  (c),  $t = 948 \mu\text{s}$  (d).

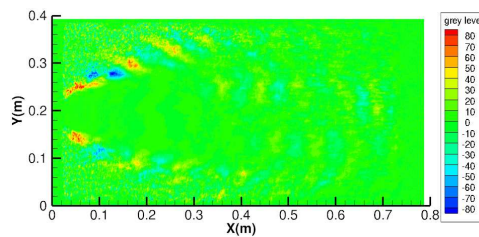


**Fig. 29.** Shape of the mode at 1734 Hz for the shadow images at  $t = 0$ .

## 6. Conclusion

The equivalence between dynamic mode decomposition and discrete Fourier transform for numerical and experimental data, based on the reduction of all the snapshots by the mean of the whole sequence, was used to propose an analytical and exact solution for the DMD, which is equivalent to the equations for the DFT. The sampling time step is assumed to be constant. The time dependant evolution of the modal shapes are a linear combination of all the reduced snapshots, the weight functions being the results of the analytical solution. This solution sets completely free from the constraint to operate matrix processings, which are expensive in time calculation and in memory size if the snapshots number is high.

The eigenvalues are completely independent of the data. They depend only on the snapshots number, and the spectral resolution is uniform. The Nyquist condition is implicitly respected. The tolerance associated with the spectral resolution is half of the resolution frequency. In order to approach the real value of a modal frequency, the

tolerance must decrease. Increasing the snapshots number is a convenient possibility, but not the sampling time step, because some information about the researched physical phenomena can be lost.

The notion of amplified or damped modes, as it is common in the original DMD analysis, does not exist here, since all the eigenvalues have a unit magnitude. The obtained modes are just preponderant or not, keeping in mind that the notion of modal growth rate is valid only in the time window of the data sequence, since the calculation does not know what happens physically before the first snapshot and after the last one. Whatever the original DMD method can reveal about the dynamical information, it is limited in the time of the observed data. Therefore, it is not unreasonable to turn towards a method, although equivalent to DFT, which presents some other significant advantages, as long as the right preponderant modes of any sequence are still detected.

This method is valid regardless of the number and the values of the snapshots. The error of this DMD analysis solution comes only from the data themselves : the time step, the snapshots number, and the snapshots values. This simple solution allows to process in a quite short time a great amount of data, the limit of which is the computer RAM size. The great advantage of the DMD is the possibility to make visible the time dependant evolution of the shapes of the selected preponderant modes. Dealing with a great number of snapshots allows, in one hand, to compensate some disadvantages outlined for the DFT, and on the other hand, to bring out better the preponderant modes and to make continuous videos of the selected modes shapes.

After an academic validation case, typically unsteady and transient, dealing with 50000 snapshots and 125000 values per snapshot, two application examples were then presented in this paper : the first one concerns some 3D CFD results (25500 snapshots, 289000 values per snapshot), and the second one concerns the images extracted from two experimental films (16000 snapshots, 524000 values per snapshot). Both cases are in current use in the field of fluid mechanics.

### Declaration of competing interest

The author declares that he has no known competing financial interests or personal relationships that could have appeared to influence the work reported in this paper.

### Acknowledgements

The author wishes to thank Yves Fabignon for encouragement to write this paper, and Nicolas Lupoglazoff and Nicolas Fdida for providing numerical and experimental data as application examples. CNES is gratefully acknowledged for permission to use both experimental films as application data in this paper. CERFACS is acknowledged as well for free use of the code AVSP in ONERA.

### REFERENCES

- [1] B. O. KOOPMAN, Hamiltonian systems and transformations in Hilbert space, Proc. Nat. Acad. Sci. USA 17(5) (1931) 315–318.
- [2] C. W. ROWLEY, I. MEZIC, S. BAGHERI, P. SCHLATTER, D. S. HENNINGSON, Spectral analysis of nonlinear flows, J. Fluid Mech. 641 (2009) 115–127.
- [3] P. J. SCHMID, Dynamic mode decomposition of numerical and experimental data, J. Fluid Mech. 656 (2010), 5–28.
- [4] J. G. F. FRANCIS, The QR transformation – A unitary analogue to the LR transformation – part 1 (1961), <http://comjnl.oxfordjournals.org/content/4/3/265.full.pdf>
- [5] J. G. F. FRANCIS, The QR transformation – part 2 (1961), <http://comjnl.oxfordjournals.org/content/4/4/332.full.pdf>
- [6] F. RICHECOEUR, L. HAKIM, L. ZIMMER, Décomposition en Modes Dynamiques - Présentation et illustrations, Laboratoire EM2C, CNRS UPR 288 - Ecole Centrale Paris (2012).
- [7] F. RICHECOEUR, L. HAKIM, A. RENAUD, L. ZIMMER, DMD algorithms for experimental data processing in combustion, Proceedings of the summer program, Center for turbulence research, Stanford University (2012).
- [8] Z. DRMAC, I. MEZIC, A. MOHR, Data driven modal decompositions : analysis and enhancements, SIAM J. Sci. Comput., Vol. 40, No. 4 (2018), pp. A2253–A2285
- [9] K. K. CHEN, J. H. TU, C. W. ROWLEY, Variants of dynamic mode decomposition : boundary conditions, Koopman, and Fourier analyses, J. Nonlinear Sci. 22(6) (2012), 887–915.
- [10] J. H. Tu, Dynamic mode decomposition : theory and applications, PhD thesis n° T-3268 (2013), Princeton University.
- [11] G. TISSOT, L. CORDIER, N. BENARD, B. R. NOACK, Analyse par « Dynamic Mode Decomposition » de mesures PIV obtenues pour le sillage d'un cylindre circulaire en régime turbulent, 13<sup>ème</sup> congrès francophone de techniques laser (2012), Rouen.
- [12] S. BAGHERI, Koopman-mode decomposition of the cylinder wake, J. Fluid Mech. 726 (2013), 596–623.
- [13] I. MEZIC, Analysis of Fluid Flows via Spectral Properties of the Koopman Operator, Annu. Rev. Fluid Mech. 45 (2013), 357–378.
- [14] J.-C. HUA, G. H. GUNARATNE, D. G. TALLEY, J. R. GORD, S. ROY, Dynamic-mode decomposition based analysis of shear coaxial jets with and without transverse acoustic driving, J. Fluid Mech. 790 (2016), 5–32.
- [15] J. C. PASCAL, Vibrations et acoustique 2, ENSIM 2A, 2008-2009 [http://perso.univ-lemans.fr/~jcpascal/Cours/ENSIM2A\\_Vibrations&Acoustique\\_2.pdf](http://perso.univ-lemans.fr/~jcpascal/Cours/ENSIM2A_Vibrations&Acoustique_2.pdf)

- [16] A. REFLOCH, B. COURBET, A. MURRONE, P. VILLEDIEU, C. LAURENT, P. GILBANK, J. TROYES, L. TESSE, G. CHAINERAY, J.-B. DARGAUD, E. QUEMERAIS, F. VUILLOT, CEDRE Software, *ONERA – Aerospace Lab Journal* 2 (2011), 11.
- [17] D. SCHERRER, F. CHEDEVERGNE, P. GRENARD, J. TROYES, A. MURRONE, E. MONTREUIL, F. VUILLOT, N. LUPOGLAZOFF, M. HUET, B. SAINTE-ROSE, P. THORIGNY, N. BERTIER, J.-M. LAMET, T. LE PICHON, E. RADENAC, A. NICOLE, L. MATUSZEWSKI, M. ERRERA, Recent CEDRE Applications, *ONERA – Aerospace Lab Journal* 2 (2011), 13.
- [18] M. PREVOST, J. CUNY, Programme d'oscillations de poussée (POP) - Programme expérimental et numérique : logique et situations étudiées, *3<sup>ème</sup> colloque R&T, Ecoulements internes en propulsion solide*, Poitiers, France (1998)
- [19] M. PREVOST, J. MAUNOURY, Y. DOMMEE, Synthèse de la base de données expérimentales instationnaires sur les essais Ariane 5 P230 et à petite échelle, *3<sup>ème</sup> colloque R&T, Ecoulements internes en propulsion solide*, Poitiers, France (1998)
- [20] N. LUPOGLAZOFF, HPCEDRE : exploitation acoustique du LP6, ONERA RT 7/24280 DMPE/DAAA (2017)
- [21] N. LUPOGLAZOFF, Simulations et exploitations complémentaires du MPS LP6, ONERA RT 9/24280 DAAA (2018)
- [22] Y. FABIGNON, J. DUPAYS, G. AVALON, F. VUILLOT, N. LUPOGLAZOFF, G. CASALIS, M. PREVOST, Instabilities and pressure oscillations in solid rocket motors. *Aeros. Sci. Techn.* 7 (2003), 191–200.
- [23] Y. DOMMEE, M. PREVOST, J. MAUNOURY, Programme d'oscillations de poussée (POP), Etude expérimentale paramétrique sur maquette de moteur à propergol solide. Résultats marquants, *3<sup>ème</sup> colloque R&T, Ecoulements internes en propulsion solide*, Poitiers, France (1998)